Design of a Small-Scale Mixing Section for a Supercritical Water Reactor through the Finite Volume Method

Kartik Tiwari

A thesis

submitted in partial fulfillment of the

requirements for the degree of

Master of Science

University of Washington

2018

Committee:

Igor V. Novosselov

John Kramlich

Per Reinhall

Program Authorized to Offer Degree:

Department of Mechanical Engineering

University of Washington

Abstract

Design of a Small-Scale Mixing Section for a Supercritical Water Reactor through the Finite Volume Method

Kartik Tiwari

Chair of the Supervisory Committee:
Prof. Igor V. Novosselov
Department of Mechanical Engineering

Supercritical water (sc-H_2O) reactors have been used for biomass gasification and the destruction of hazardous waste. Laboratory scale reactors are typically used for development of chemical kinetic rate parameters. These smaller reactors with lower Reynolds numbers often suffer from slow mixing between the reagent and sc-H_2O; this slow mixing increases uncertainty in the data required for calculation of chemical kinetic rate parameters. In this study, we present a multiple-jet in crossflow design for a mixing section, which enables rapid mixing of reagents into sc-H_2O. A parametric analysis is conducted to establish an optimum jet-to-crossflow velocity ratio (r) for scalar mixing using three-dimensional computational fluid dynamics (CFD) with Detached Eddy Simulations (DES) for resolving turbulence. Kinetic theory models for calculating physical properties of the fluids at the supercritical state are evaluated against data available in published literature. CFD simulations show that mixing can be characterized by three distinct regimes: (i) under-penetrating jets, (ii) weakly penetrating jets, (iii) jets forming

counter-rotating vortex pairs (CVPs), and (iv) impinging jets. The best mixing is observed for jets forming CVPs; under-penetrating jets show the worst mixing. The mechanism of mixing in the three configurations is explained. Decomposition of methanol (MeOH) in a continuous-flow sc-H_2O reactor is simulated with CFD using global first-order chemical kinetic rate parameters calculated from published experimental data. This numerical modeling sheds insight into the complex physiochemical processes of organic compound decomposition in the supercritical environment. The modeling approach can be used in industrial process optimization and to improve the design of new and existing systems.

Table of Contents

List of Figures

List of Tables

Nomenclature

r	=	Velocity ratio of a jet to crossflow
J	=	Momentum flux ratio of a jet to crossflow
CVP	=	Counter-rotating vortex pairs
d_m	=	Diameter of main pipe
d_j	=	Jet diameter
U	=	Mean velocity
ρ	=	Density
D	=	Binary diffusion coefficient
T	=	Temperature
M_w	=	Molecular weight
P	=	Pressure
σ	=	Lennard Jones energy parameter
Ω_D	=	Diffusion collision integral
μ	=	Dynamic viscosity
$\Omega\mu$	=	Viscosity collision integral

T_r	=	Reduced temperature
P_r	=	Reduced pressure
ρ_r	=	Reduced density
ID	=	Internal diameter
v_t	=	Turbulent viscosity
k	=	Turbulent kinetic energy
ε	=	Turbulence dissipation rate
l_{DES}	=	DES length scale
C_{DES}	=	DES model constant
Δ_{max}	=	Maximum grid size
v	=	Kinematic viscosity
$U_{i,j}$	=	Velocity gradient
A	=	Pre-exponential constant
E_A	=	Activation energy
R	=	Gas constant
j	=	Diffusion flux
m_D	=	Diffusion mass transfer

w = Species concentration

$\vec{v}$ = Velocity

A = Area

t = Time

Y = Mass fraction of the species

$\overrightarrow{v_z}$ = Velocity along z-direction

Subscript p,q = Property of p^{th} or q^{th} species

Subscript k = Value at the k^{th} control area

Subscript j = Jet parameters

Subscript m = Crossflow parameters

Subscript c = Critical point parameters

Acknowledgment

I extend my warm thanks to my advisor Dr. Igor Novosselov for giving me an opportunity to work under his supervision. There are few people as sincere and enthusiastic while guiding others. Without him, this project would not have reached its conclusion. I would like to thank my committee members, Professor John Kramlich and Professor Per Reinhall for their constant insights and suggestions. Professor Kramlich provided necessary insights on chemical kinetics and thermodynamics, essential in completing this thesis. I am also thankful to Professor James Riley for navigating me through the quagmires of turbulence and its modeling.

I would also like to extend my gratitude to my lab mates, especially, Davis Gorman, Brian Pinkard, Justin Davis, Arjun Athreya, Patrick Fillingham, and Yifei Guan for their advice, enriching discussions, and occasional rounds of beer. Without them, it would have been difficult to endure long days and nights in a lonely basement.

Most importantly, I extend my gratitude to my family and friends for their encouragement and support at best and worst of my times. Special thanks to my parents and brothers for being a constant source of inspiration.

Lastly, I am thankful for the funding provided by the DOD Defense Threats Reduction Agency – Grant HDTRA1-17-1-0001, as well as the resources provided by the University of Washington which made this work possible. This work was facilitated through the use of advanced computational, storage, and networking infrastructure provided by the Hyak supercomputer system and funded by the STF at the University of Washington.

Chapter 1. Introduction

Water near and above its critical point provides unique physical and chemical properties making it a suitable medium for conducting multiphase reactions of organic compounds with negligible environmental impact [1]. The weakening of hydrogen bonds reduces the dielectric constant of water, thereby, increasing the solubility of non-polar organic compounds and gases [1]. Moreover, the physical properties of supercritical water (like density and viscosity) can vary over a wide range depending on the operating pressure and temperature [1, 2]. The high temperature and pressure of supercritical state also helps to increase the rates of chemical reactions.

Sc-H_2O reactors are being successfully used for many applications, ranging from biomass gasification to the destruction of toxic organic waste [3-7]. These reactors exist in batch as well as continuous flow configurations. Continuous-flow sc-H_2O reactors provide better process control, higher throughput, better scalability, and reduced residence time requirements compared to batch reactors [8]. Many reactors use a premixed slurry of water and the organic reagent, but this can lead to the formation of tars and char in the heating section via pyrolysis [9]. In chemical kinetic studies, the ambiguity about the reaction onset also introduces uncertainty in determining the reaction residence time. Post-critical mixing, where reagents are mixed into water already above the critical point, can suffer from mixture non-homogeneity, especially in small-scale reactors due to low Reynolds number flows [10]. Several passive and active mixing systems have been proposed for rapid mixing of fluids in such small-scale reactors. Many review papers provide a good summary of such microscale mixing systems [11]; jet-based systems are preferred due to the simplicity of design, fast mixing, and reduced cost. Jet-based systems improve the mixing of the

fluids by inducing turbulence and increasing the diffusion surface area between the fluid streams [11].

Traverse jet mixers, where the solute is injected perpendicular to a crossflow of solvent, lead to better mixing and entrainment than free jet mixers [12]. A multiple-jets-in-crossflow (MJC) mixer consists of radially symmetric jets perpendicular to a tube or duct carrying the bulk flow. Multiple jets reduce the mixing time by increasing the diffusion area between the fluids [13-15]. Extensive numerical and experimental analysis has been performed for describing the flow dynamics and mixing, primarily, for a single jet in crossflow [12, 16-18]. Equations 1 and 2 provide two non-dimensional parameters, the momentum ratio (J) and the velocity ratio (r) used to define jets in crossflow.

$$J = \frac{\rho_j U_j^2}{\rho_c U_c^2} \tag{1}$$

$$r = \frac{U_j}{U_c} \tag{2}$$

Figure 1 shows large-scale vortex structures (like CVP), horseshoe vortices, and hairpin vortices formed by the interaction of a single jet with a crossflow [12, 19]. The crossflow modifies the vorticity of the jets leading to the formation of CVP downstream of the jet exit. Kelso et al. studied single round jets in crossflow using flow visualization techniques and postulated that the roll-up of the jet shear layer initiates the CVP [20]. Based on large-eddy simulations, Lester et al. linked the formation of CVP with the appearance of a quasi-steady hanging vortex pair close to the jet exit [16]. Sau and Mahesh performed detailed Direct Numerical Simulations (DNS) of single jets in planar crossflow and found that the formation of CVP is governed by the velocity ratio (r) [21]. A single jet in a laminar crossflow do not form CVP for low velocity ratio jets (r <

2) [21, 22]. The development of CVP delays with the increase in velocity ratio of jets [12]. Apart from enhanced entrainment due to CVP formation downstream of the jet, traverse jets lead to a faster mixing in the near field when the jet has not yet bent by the crossflow. Muddipi and Mahesh accredited this enhanced mixing to the deformation of the jet cross-section at the downstream of the jet by the crossflow. This leads to a pressure gradient that entrains more crossflow fluid into the jet [23].

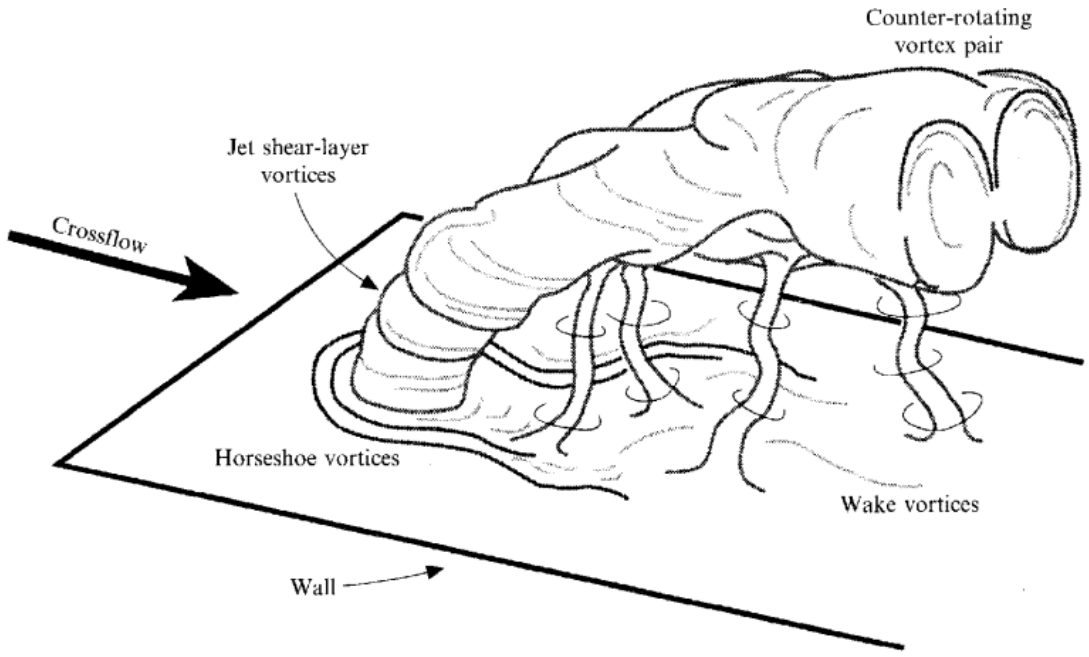

Figure 1. Schematic showing different vortex structures observed in a single jet in crossflow, from Fric and Roshko [24].

An MJC mixer displays most of the flow features of a single jet in crossflow. However, the interaction of jets with each other modifies the flow and mixing dynamics. The initial research of the mixing in an MJC mixer was linked to application in gas turbine combustors [15, 25, 26]. Holdeman et al. summarized the early NASA supported experimental and computational results on MJC mixers for round tubes [15]. They found that the jet penetration and mixing rate depends

on the jet to crossflow momentum flux ratio (J), number of orifices, orifice shape, and orifice spacing. The mixing rate improved with an increased in J until it reached an optimum value, further increase in J lead to a decline or no further increase in the mixing rate. Recently, the MJC has been applied for mixing in small-scale chemical reactors for production of nanoparticles and pyrolysis of hydrocarbons [27-29]. Luo et al. studied the performance of small-scale MJC mixers for liquids in the fully developed turbulent regime, experimentally with Planar Laser Induced Fluorescence (PLIF) and numerically with LES [13, 14]. The diameter of the main pipe was in the range of 16 mm – 21 mm. They observed that mixing improves with the number of jets, due to increase in peak value and distribution of vorticity in the flow. For their configuration, the jets collided at $r > 5$, which lead to a decrease in the mixing time. They attributed the greater mixing time to backflow within the impinging of jets. However, the authors did not explain the mixing mechanism for different jet trajectories and the causes for improvement in mixing rate with the increase in velocity ratio.

CFD modeling of such flows with basic Reynolds Averaged Naiver-Stokes (RANS) and Reynolds Stress (RSM) models have been shown to deviate considerably from the experiments [29-31]. These models must be calibrated with the experimental data to provide acceptable results. Numerical simulations of single jet in crossflow with RANS models overestimate jet penetration and underestimate jet width [31]. LES and DNS simulations have shown better results in modeling such flows. However, DNS simulations are still limited to low Re flows, and the excessive computational cost makes it infeasible to apply for a parametric study and in complex geometries. LES simulations enable shorter convergence times, but the need to resolve the boundary layer make these models computational expensive for many practical engineering applications. Delayed Detached Eddy Simulations (DDES) can provide a middle ground between RANS and LES/DNS

methods [32-35]. In DDES the turbulent length scales near the walls are modeled with RANS based approach, and the separated flow is resolved using sub-grid scale models based on LES approach. CFD simulations with DES modeling show considerable improvement in resolving transient and coherent features of the flow than the RANS models [34]. Yin et al. showed that the DES method could successfully resolve most of the coherent flow features and mixing dynamics for a single jet in crossflow [35].

Most studies focus on the mixing of fluids at moderate to large Reynolds numbers (*Re*). However, most of the small scale sc-H_2O reactors operate at low *Re*, in the laminar to transition turbulent regime. Since the turbulence in the pipe flow influences the mixing rate, it is necessary to evaluate the performance of MJC at low to moderate *Re* flows. The mixing and flow dynamics also depend on fluid properties, and the scientific literature does not provide information about the applicability of MJC in a supercritical water environment. The objective of this study is to design a small-scale mixing section for a supercritical water reactor operating in laminar to transitional turbulent flow regime. The mixing rate must be faster than the decomposition rate of most organic compounds in sc-H_2O to allow plug flow conditions in the reactor [8, 36, 37]. The mixing rate of a small-scale MJC for a laboratory scale sc-H_2O reactor is investigated with finite volume CFD using transient DDES method. The validity of the kinetic theory model for calculating the binary diffusion coefficients and viscosity of the fluids in their supercritical state is evaluated. Later the model is incorporated in CFD analysis to design an MJC mixing section for a laboratory sc-H_2O reactor. The mixing mechanism is explained, and optimum design for mixing section is established.

Chapter 2. Kinetic Theory Model

To model the flow physics and the interaction between the reactants, it is essential to correctly estimate the transport properties of the fluids in the supercritical state. These properties can vary significantly with temperature, pressure, and composition [38, 39]. High temperature and pressure make an experimental evaluation of the fluid properties for a wide range of operating conditions challenging. The kinetic theory of gases provides one approach for estimating these properties for engineering applications. However, the validity of the kinetic theory for supercritical fluids needs evaluation [37]. Here the use of kinetic theory to predict the binary diffusion coefficient and viscosity of benzene in water is evaluated in the supercritical region. Benzene is one of the intermediates in the SCW decomposition of lignin, cellulose, glucose, and biomass [36]. The experimental data for binary diffusion coefficient [38] and kinetic theory parameters [40, 41] have been presented in the literature. Equation 3 shows the formula for calculating the binary diffusion coefficient for species p in species q. It is based on the modified Chapman-Enskog theory of kinetic gases [41, 42]. The equation is derived by solving the Boltzmann equation for velocity distribution [43]. The diffusion collision integral (Ω_D) considers the effects of intermolecular forces between the gas molecules. The intermolecular force between the colliding molecules is calculated from the Lennard-Jones potential function [41].

$$D_{pq} = 0.00188 \times \frac{\left[T^3\left(\frac{1}{M_{w,p}}+\frac{1}{M_{w,q}}\right)\right]^{1/2}}{P\sigma_{pq}^2\Omega_D}. \quad (3)$$

Equation 4 gives the formulation of viscosity based on similar modified Chapman-Enskog theory for symmetrical hard spheres using Lennard-Jones potential function. The viscosity predictions are independ of the fluid pressure.

$$\mu_p = 2.67 \times 10^{-6} \frac{\sqrt{M_{w,p}T}}{\sigma_p^2 \Omega_{\mu,p}}. \quad (4)$$

These equations are easy to use in a numerical scheme, they apply universally for most gases, though best at high temperature and low pressure. Several authors have suggested more accurate and involved methods to predict properties of gas and liquids at high temperature and pressure [43, 44]. However, most of these methods are difficult to link to a numerical scheme and apply in a narrow range of temperatures and pressures. He and Yu suggest such a method to predict binary diffusion coefficient of solutes in supercritical fluids at infinite dilution [45]. It can be applied for solvents in the temperature and density ranges of $0.66 < T_r < 1.78$ and $0.22 < \rho_r < 2.62$ respectively.

The literature contains limited data for the binary diffusion coefficient of benzene in water above the critical point. The highly corrosive, oxidative nature of sc-H_2O make an experimental evaluation of such properties challenging [38, 39]. Non-intrusive techniques like Taylor dispersion technique or Raman spectroscopy might help to fill the vast gaps in the available experimental dataset. Nevertheless, until then, the most viable technique to obtain reliable data can be through detailed molecular dynamics simulations. Nieto-Draghi et al. calculated the properties of the benzene-water mixture at two thermodynamic states above the critical point using such detailed simulations [38].

Table 1 compares the binary diffusion coefficient of a super-critical benzene-water mixture predicted by kinetic theory with published data and correlation proposed by He and Yu [38, 45]. The calculated viscosity of water is compared with the NIST database [46]. The predicted and the published properties of the fluids are in the same order of magnitude. The operating conditions for the simulations are 25 MPa and 923 K. At low pressures, the data and theoretical calculations for

both diffusion coefficient and viscosity agree better than at high pressures. Viscosity predicted by kinetic theory agrees well with NIST data for the operating condition of the reactor; the error is less than 5%. The error in viscosity prediction increases with pressure, as equation 4 contains no information about pressure or density of the fluid. Limited published data for diffusion coefficient makes direct verification of kinetic theory difficult. In an attempt to extend the dataset, the diffusion coefficient at the specified temperatures and pressures are also calculated by the method of He and Yu [45]. The calculated diffusion coefficient by the He and Yu method is in good agreement with the published data at 55.29 MPa. However, the value diverges at 668.1 MPa as the temperature and pressure are beyond the prescribed range for this method. Kinetic theory shows acceptable agreement with the published and calculated dataset. The introduction of additional tuning parameters like density and ionic interactions into the kinetic theory calculations can improve the model accuracy for supercritical fluids. However, comprehensive data sets to validate such approaches have not been developed. This task is beyond the scope of this project but will be considered as a future research direction. Since the operating pressure for most sc-H_2O reactors is less than 55 MPa, the kinetic theory model likely can be used for CFD modeling. However, more robust experimental data and analytical modeling are required to generalize these conclusions. In

Table 1. Comparison of the binary diffusion coefficient and viscosity of water with the published properties **[38, 46]**. Benzene mole-fraction - 0.1

Pressure (MPa)	Temperature (K)	Diffusion Coefficient			Viscosity	
		Nieto-Draghi [38] ($\times 10^{-8}$ m^2/s)	Method of He and Yu [45] ($\times 10^{-8}$ m^2/s)	Kinetic theory ($\times 10^{-8}$ m^2/s)	NIST database [46] ($\mu Pa \times s$)	Kinetic theory ($\mu Pa \times s$)
25	673	-	8.21	12.96	29.19	29.51
25	923	-	18.14	23.34	38.31	40.15
55.29	673	3.11	2.9	5.81	77.31	29.51
686.11	673	1.05	0.2	0.48	130.00	29.51

this study, the diffusion coefficient and the viscosity of the fluids will be modeled using kinetic theory.

Chapter 3. Computational Model

3.1 Computational Domain

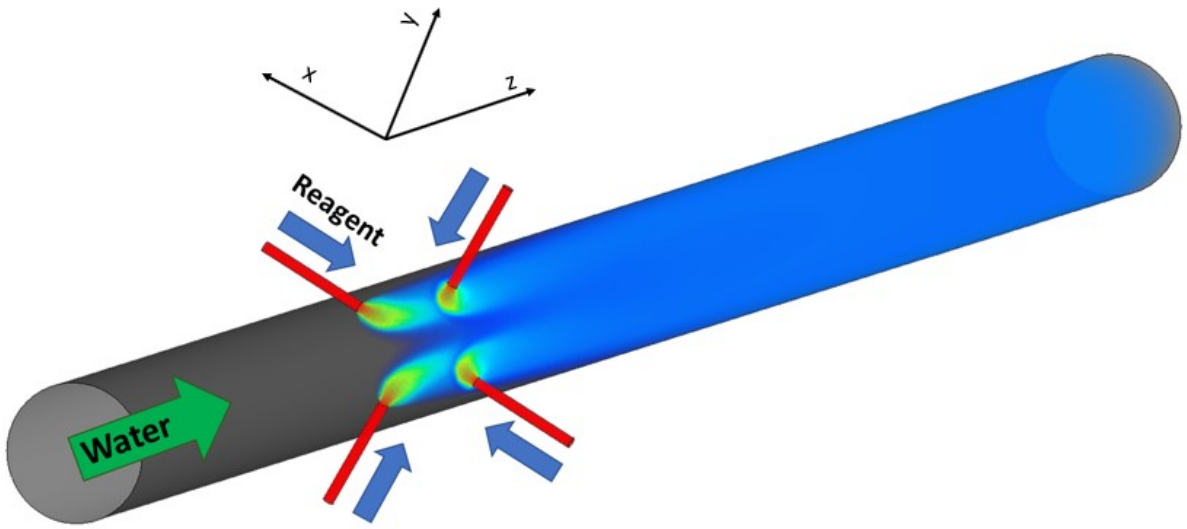

Figure 2. Schematic for multiple jets in a crossflow mixer with four jets. The volume rendering shows reagent mass fraction. The figure is not drawn to scale.

Three-dimensional CFD analysis is used to optimize the mixing of supercritical fluids in an MJC mixer. **Figure 2** shows a schematic of the geometry. The sc-H_2O at 923 K flows at 2.19 kg/s through the pipe ID 3.05 mm. Benzene at 923 K (10% by mass of water) is injected through the four perpendicular round inlets; the diameter of the injection tubes is varied in the parametric study. A mass flow boundary condition is specified at the benzene and water inlets. The outlet is modeled as pressure outlet boundary with 25 MPa. Benzene is injected at 10 d_m from the water inlet to allow velocity profiles to develop before the jet injection. The length of the jet inlet tubes is greater than 10 d_j for the same reason. The main pipe extends for 120 mm (~40 d_m) from the jet injection plane. **Figure 2** also shows the global coordinate system. The center of the domain lies at the axis of the main pipe where the axes of four jets intersect geometrically.

The numerical grid consists of ~2 million tetrahedral elements. The maximum cell skewness is maintained below 0.85. Six prism layers (inflation layers) are maintained normal to the flow near the wall to model the boundary layer dynamics accurately. Both fluids are injected at supercritical state (923 K and 25 MPa). The densities are taken from the NIST database whereas kinetic theory calculates the viscosities and diffusion coefficients.

3.2 Numerical Scheme

Table 2. Summary of Numerical Methods

Grid	3D tetrahedral elements
Number of cells	~2,000,000
Solver	Pressure based transient solver
Compressibility effects	Excluded
Buoyancy effects	Excluded
Mixture Density	Volume weighed mixing law
Mixture Cp	Mixing law
Mixture Thermal conductivity	Mass weighed mixing law
Mixture Viscosity	Mass-weighted mixing law
Mass diffusivity	Kinetic theory
Pressure-Velocity Coupling	Coupled
Transient formulation	Bounded second order Implicit
Pressure	2nd order numerical algorithm
Momentum	Bounded central differencing
Density	2nd order upwind algorithm
Turbulence	2nd order upwind algorithm
Species	2nd order upwind algorithm
Energy	2nd order upwind algorithm

The numerical simulations are performed on ANSYS Fluent 18.2 [47]. Transient CFD solves the three-dimensional Naiver–Strokes, energy, and species transport equations. The conservation equations are discretized based on finite volume methods. Delayed detached eddy simulation (DDES) method is used to model flow instabilities and potential transition to turbulence at high jet velocity conditions [32]. The turbulence model is explained later. **Table 2** summaries

the numerical scheme used in the simulations. Since the Mach number of the flow is low and compressibility effects can be neglected, a pressure-based solver is used. The pressure-based method solves a pressure correction equation derived from the continuity and momentum equations. The calculated velocity field, when corrected by pressure, satisfies the continuity equation. ANSYS Fluent contains two pressure-based solver algorithms: (i) Segregated solver and (ii) Coupled solver. In the segregated solver scheme, the governing equations are solved sequentially. As the name suggests, the coupled scheme simultaneously solves the continuity and momentum equations. However, other equations are solved sequentially like the segregated solver. A coupled solver helps to reduce the number of iterations required to reach a converged solution. Second order upwind schemes are used to interpolate the face values from the cell centers except for momentum. A bounded second order central differencing scheme is used to interpolate momentum at face centers of the cells. Central differencing scheme allows very small numerical diffusion across the cells and are thus ideal for LES -DES types turbulence schemes [47]. Bounded second-order implicit scheme integrates the discretized governing equations over time. An implicit scheme is unconditionally stable concerning time step size. The time step size for each case is maintained such that flow courant number is near unity (based on the highest velocity in the domain). The density of the fluids is taken from the NIST database [46], and the viscosity and diffusion coefficient is calculated from kinetic theory as explained in Chapter 2. The mixture properties depend on the mixture composition, calculated using mixing laws as specified in **Table 2**.

3.3 Turbulence model

Transient Delayed Detached Eddy Simulation (DDES) is used to resolve the turbulence in the flow. DDES is a hybrid RANS/LES scheme, where the near wall region is modeled with

unsteady RANS and other regions of the flow are resolved using LES based schemes. LES methods have been shown to work best in resolving the core turbulent region with energy containing large-scale eddies, and the RANS models have shown to predict the boundary layer dynamics with sufficient accuracy. DDES thus combines the best features of both the models for predicting the onset of turbulence and relaminarization. Detached-Eddy Simulation (DES) was proposed by Spalart and other in 1997 for modeling boundary separation in external flows with large Reynolds number [48]. Since then interest in DES method has been successfully applied in numerous internal and external flows scenarios, e.g., [34, 49, 50].

The RANS based realizable *k-ε* turbulence model is used to model the wall boundary flow. RANS schemes solve the averaged conservation equations to give mean velocity profile and scalar concentrations. The Reynolds stresses that occur due to averaging of equations are modeled based on turbulent viscosity concept or through Reynolds-stress transport equations. *k-ε* is a two-equation model, based on turbulent viscosity concept that assumes scalar flux vector or Reynolds stress anisotropy to lie in the direction of mean scalar gradient or mean velocity gradient [51]. The model solves transport equations for two turbulent quantities: turbulent kinetic energy (*k*) and turbulence dissipation rate (*ε*) [47]. The turbulent viscosity is then calculated from *k* and *ε* as:

$$\nu_t = C_\mu k^2/\varepsilon \tag{5}$$

Where, C_μ = 0.09, is one of the model constants [51].

The turbulent viscosity can then be used to model the Reynolds stresses, thus, closing the model. *k-ε* is one of the most robust and widely used RANS models. It has shown considerable accuracy in predicting internal and wall-bounded flows. The averaging operation, however, loses some of the details of the three-dimensional eddies, which carry most of the information in a

turbulent flow. Several authors have also argued about the impractical theoretical assumptions of these models, e.g., [34, 51]. For most of the application, RANS models need to be calibrated with the experimental data to provide reasonable results. Most of these concerns are resolved by Large Eddy Simulations (LES).

In Large Eddy Simulation (LES), the large-scales of turbulence are directly resolved while the small scales are modeled with sub-grid scale schemes. It is based on the premise that large-scales of turbulence are geometry driven while the small scales are relatively universal and isotropic [51, 52]. The large scales are also responsible for transport of most of the mass, momentum, and passive scalars. The equations of motion are filtered by a filtering function to derive the resolvable-scale equations. Typically, a box filter, with the filter width equal to the grid spacing, is used. The filtering operation gives unresolved sub-grid scale stresses as Reynolds stresses in RANS averaging. These stresses are then modeled using a subgrid scale model. The dominance of viscosity at the boundary layer reduces the scale of turbulence near the walls. To resolve the boundary layer near the walls, the mesh size must be so small that LES effectively becomes DNS; it makes application of LES for simulating such flows computationally infeasible.

In DES wall bounded regions are modeled using RANS based schemes and the large scales of turbulence are resolved using LES approach. The blending between the RANS and LES modes is achieved by modifying the dissipative term of the kinetic energy equation in the k-ε model. The model distinguishes between the LES and RANS mode based on two critical length scales: the RANS length scale (l_{RANS}) and LES length scale (l_{LES}). Equation 6 shows the modified dissipation term (Y_k), where l_{DES} is the length scale for DES.

$$Y_k = \frac{\rho k^{\frac{3}{2}}}{l_{DES}}. \tag{6}$$

The minimum of the RANS and LES length scale is selected as the DES length scale:

$$l_{DES} = \min(l_{RANS}, l_{LES}), \tag{7}$$

where,

$$l_{RANS} = \frac{k^{\frac{3}{2}}}{\varepsilon}, \tag{8}$$

$$l_{LES} = C_{DES}\Delta_{max}\,. \tag{9}$$

Therefore, for cells with $l_{RANS} < l_{LES}$, the turbulent scales are considered unresolvable, and RANS schemes are used to model these scales. The above formulation is simple and has shown good prediction accuracy for large Reynolds number heavily separated flows [34]. However, it can lead to incorrect behavior in thick boundary layer regions. When the boundary layer thickness becomes less than the grid spacing parallel to the wall, the grid spacing becomes fine enough to activate the LES mode. However, the grid spacing is not fine enough to accurately resolve viscosity dominant turbulence in this region. The DES method then predicts lower eddy viscosity than pure RANS models [32, 53]. The net Reynolds stresses do not represent LES or RANS mode and can lead to premature separation. To avoid this behavior, Spalart et al. suggested modifying the l_{DES} to retain the RANS model within the boundary layer even when the boundary layer thickness is more than grid spacing [32]. They named this formulation as Delay Detached Eddy Simulation (DDES). The modified l_{DES} is defined as:

$$l_{LES} = l_{RANS} - f_d(0, l_{RANS} - C_{DES}\Delta_{max}) \tag{10}$$

Where f_d is the blending function given by:

$$f_d = 1 - \tan((20r_d)^3) \quad (11)$$

Here, r_d is a non-dimensional distance from the wall and is given by equation 12. d_w is the distance from the wall and κ is a model constant equal to 0.41.

$$r_d = \frac{(\nu_t + \nu)}{\sqrt{U_{i,j}\,U_{i,j}}\kappa^2 d_w^2} \quad (12)$$

3.4 Decomposition of Methanol

The experimental data of Hack et al. for MeOH decomposition [54] is used to derive the rate parameters, the authors provide MeOH concentration data over a range of temperatures and residence times and suggest that MeOH decomposition can be modeled with the overall global reaction given by (13). The reaction rate was assumed to be independent of the initial MeOH concentration in the mass fraction range of 0.002 to 0.004.

$$CH_3OH + H_2O \rightarrow CO_2 + 3H_2 \quad (13)$$

Equation 14 shows the first-order kinetic rate equation used to model the decomposition of MeOH in the reactor. It is assumed that rate of MeOH decomposition only depends on the concentration of MeOH and temperature, as the relative change in concentration of water is negligible.

$$\frac{d[CH_3OH]}{dt} = A \times exp\left(-\frac{E_A}{RT}\right) \times [CH_3OH] \quad (14)$$

Based on the data from [54], we calculated the activation energy and the pre-exponential constant of 147.96 kJ/mole and 1.94E+10 s^{-1} respectively; these rate parameters are used in CFD. Equation *3* is used to calculate the binary diffusion coefficient while other fluid properties are taken from the NIST database.

Chapter 4. Results

The MJC mixer was optimized to achieve the fastest mixing of the fluids by varying the diameter of the jets. The flowrate and diameter of the crossflow are kept constant in all the simulations. The *Re* of the cross-flow (based on main pipe diameter and mean velocity) is 6700, suggesting a transition to the turbulent regime. **Table 3** summarizes the jet characteristics for each simulation. The diameter of jet governs the momentum flux ratio (*J*) between the jet and the crossflow. The momentum flux ratio (*J*) influences the mixing rate and the large-scale flow features of an MJC mixer [12, 14, 15]. For all the simulations, the density of the fluids is constant, and *J* can be reduced to *r*. The jet diameter is varied from 0.09 mm to 0.60 mm and Reynolds number (based on jet diameter and mean jet velocity) from 670 to 4526, covering the laminar to transition (to turbulence) regimes. According to the jet trajectories observed, the cases are classified into four categories: i) Under penetrating jets (UPJ), ii) Weakly penetrating jets (WPJ), iii) Jets forming CVP (JCVP), and iv) Impinging Jets (IJ). These jet trajectories are explained later.

Table 3. Jet parameters for the cases simulated

Case	Velocity ratio (*r*)	Momentum ratio (M)	Jet inlet diameter (mm)	Reynolds number of jet	Jet trajectory
1	0.22	0.005	0.60	670	Under-penetrating jets (UPJ)
2	0.88	0.022	0.30	1341	Weakly penetratig jets (WPJ)
3	1.26	0.032	0.25	1609	Jets forming CVP (JCVP)
4	2.73	0.068	0.17	2367	
5	8.00	0.198	0.10	4024	Impinging Jets (IJ)
6	10.00	0.250	0.09	4526	

4.1 Large-scale flow features of an MJC mixer

The influence of jet diameter and velocity ratio on the large-scale flow features of MJC mixers is discussed in this section. **Figure 3-a** shows the path-lines of the flow originating from the jet inlet with the z- vorticity contours at 10 mm from the injection plane (end-view from water inlet). The jets under-penetrate for lower *r* values (Case 1) as the inertia of the jets is significantly lower than the crossflow. The fluid from the jet is trapped in the boundary layer of the crossflow and does not result in significant flow vorticity (see colored vorticity contours). **Figure 3-b** shows the velocity contours at the midplane along the axis of the pipe. The under-penetrating jets slightly modifies the velocity profile of the crossflow. It creates a small wake region at the leeward side of the jet and locally accelerates the crossflow at the core of the pipe. The penetration of the jets improves with increased velocity ratio. However, no CVP are observed for $r < 1$ (Case 2). These jets are characterized as weakly penetrating jets. These results are consistent with the numerical and experimental analysis for a single jet in crossflow, which shows the absence of CVP formation for low-velocity ratio jets [12, 21, 22]. For $r > 1$ (Cases 4 and 5), full developed CVPs are observed downstream of the jets, and significant z-vorticity is induced in the flow. In the mixing section design, four pairs of counter-rotating vortices are formed, one for each jet. These jets are termed as jet forming CVP (JCVP). Velocity contours also show a larger wake region and considerable acceleration of the flow downstream of the jet inlet for jets forming CVP. These jets penetrate significantly in the crossflow and merge with cross flow without significant interactions with each other. At sufficiently high-velocity ratios (case 7 and case 8), the jets have enough momentum to penetrate the crossflow and impinge at the center, making the flow chaotic and turbulent. These jets are referred as Impinging Jets (IJ). The larger Re (based on nozzle diameter and mean jet velocity) of the jets also triggers the turbulence in the crossflow. This local turbulence decays if

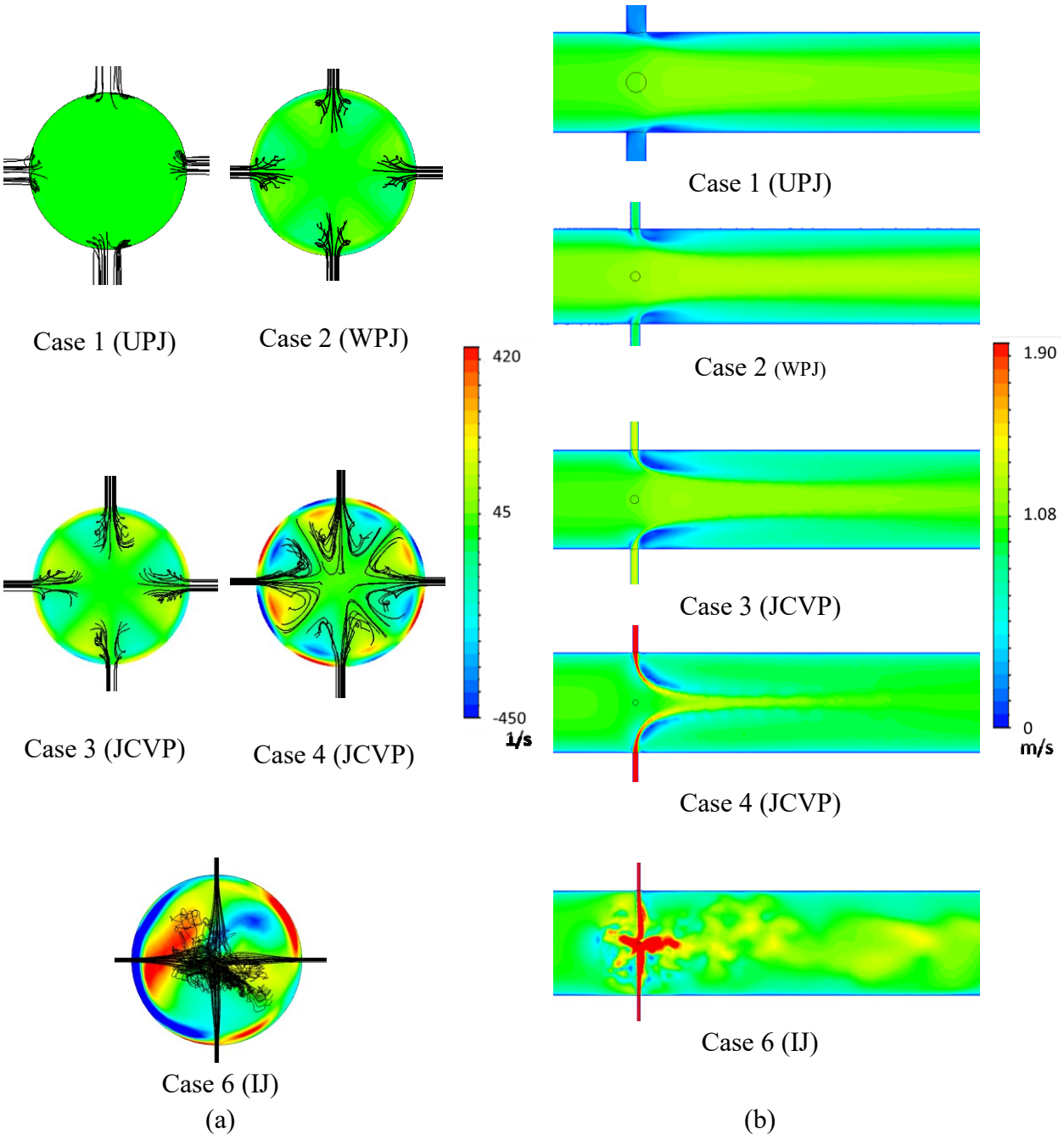

Figure 3. (a) Path-lines of flow (in black) originating at jet inlets along with the instantaneous vorticity contour at a cross section 10 mm from the jet inlet for specified jet parameters. The strength of counter-rotating vortices increases with the velocity ratio until the jets impinge and make the flow chaotic. (b) Velocity contours at the midplane along the length of the axis.

the pipe *Re* is in the laminar region. Counter-rotating vortices were not observed for the IJ cases. The origin of CVPs is linked to the reorientation and folding of cylindrical vortex sheet formed at the jet exit [18, 20]. Upon the impingement, the jets dissipate their momentum and lose their initial vorticity which hampers the formation of CVPs. The vorticity contours show that the vorticity in the flow is random and does not suggest the formation of any large-scale coherent vortex structures.

For a single jet in crossflow, wake vortices (see Figure 1) are observed downstream of the jet [12]. These are upright vortices and are formed due to flow separation in the crossflow boundary layer at the vicinity of the jet. Figure 4 shows the contours of invariant Q criterion at a plane parallel to the y-z plane, at x= 1.2 mm), and streamlines (solid black lines) originating from one of the jet inlets for each jet trajectory. The streamlines show the bending of the jets with the crossflow. As observed before, the jets with the lowest velocity are bent the most, and the influence of crossflow on the jet trajectory reduces with the increase in *r.* Large positive values of Q criterion indicate dominant vortex structures and large negative values indicate high dissipation rate (strain rate). The under-penetrating jets (case 1) show negligible Q values around the jets, suggesting the absence of vortex structures in the flow. Weakly penetrating jets (case 2) and jets forming CVP (case 5) show high dissipative region just upstream of the jet at the stagnation point. This is the region where the crossflow encounters the jet and difference in velocity leads to the formation of this high strain dissipative region. However, the high Q values downstream of the jets suggest a wide but short wake region for weakly penetrating jets. Such broad and open wakes are also observed by Fric et al. for low-velocity ratio jets in their flow visualizations of the single turbulent jet in crossflow. For the jet forming CVP (case 5), two lopes of high vorticity region are observed downstream of the jets. These lopes suggest the formation of fully developed wake vortices seen

for single jets in crossflow. Many authors have suggested that the reorientation of these "hanging" vortices formed downstream of the jet leads to the formation of CVP [16, 20]. The absence of these "hanging" vortices can be the possible reason why CVPs are not observed for other jets. These

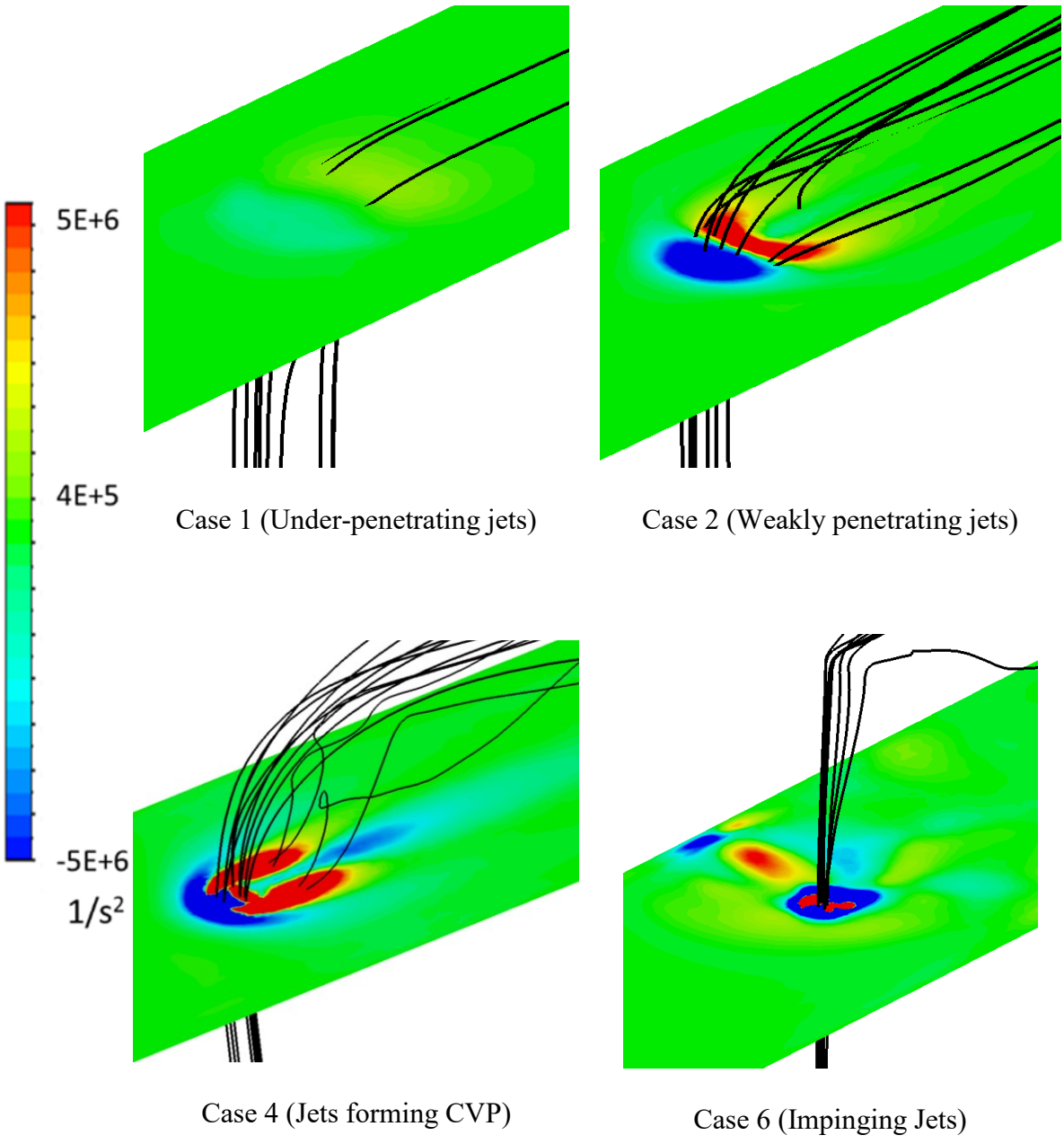

Figure 4. Instantaneous contours of invariant Q criterion and the streamlines originating from one of the jet inlets.

vortex structures also lead to significant entrainment and mixing in the vicinity of the jets [55]. Finally, Q values for impinging jets (case 8) are chaotic and random. A high strain region wraps around the jet due to its high velocity, accompanied by a small region of high vorticity. Small vortex regions are instantaneously formed and destroyed due to chaotic nature of the flow.

4.2 Optimum mixing configuration

It is useful to revisit the basic principles of mixing before discussing the results in detail. The Fick's law gives the diffusion flux transfer of a species per unit area driven concentration gradient. For diffusion of any species 'p' in species 'q'. It is expressed as:

$$j_p = -D_{pq}\nabla w_p. \tag{15}$$

By re-arranging (15), the diffusion mass transfer can be expressed as:

$$m_D = D_{pq} \cdot A_{pq} \cdot \nabla w_p. \tag{16}$$

Equation 16 gives the diffusion mass transfer for any species, where "A" is the diffusion area between the two fluids. It shows that the diffusion mass transfer between the species increases with the diffusion area. The diffusion rate improves with the increase in diffusion area, diffusion coefficient, and concentration gradient. Stretching and deformation of the fluid element by turbulence in the flow improves the mixing rate by increasing the effective diffusion are between the fluids.

Equation 17 gives the uniformity index (UI) weighted by mass flow rate. It quantifies the variation of species flux over the cross-section of the flow. UI values close to unity represent a homogeneously mixed state, and values close to zero completely segregated flow.

$$UI = 1 - \frac{\sum_{k=1}^{n}[(|Y_k - Y|)(|\rho_k \overrightarrow{v_k} A_k|)]}{2|Y| \times \sum_{n}^{k}(|\rho_k \overrightarrow{v_k} A_k|)}. \quad (17)$$

Figure 5 shows the time-averaged UI of benzene along the axial distance which is non-dimensionalized by the pipe diameter (D). UI is calculated at 20 sections along the axis of the pipe at each (converged) time step and ensemble averaged over the all instances. The UI improves with the axial distance for all the cases, rapidly at first, then slowly later as the uniformity of the mixture improves. The worst performance of the mixer occurs with the under-penetrating jet (case 1). However, a UI of 0.9 is reached in 5D which might be sufficient for many engineering applications.

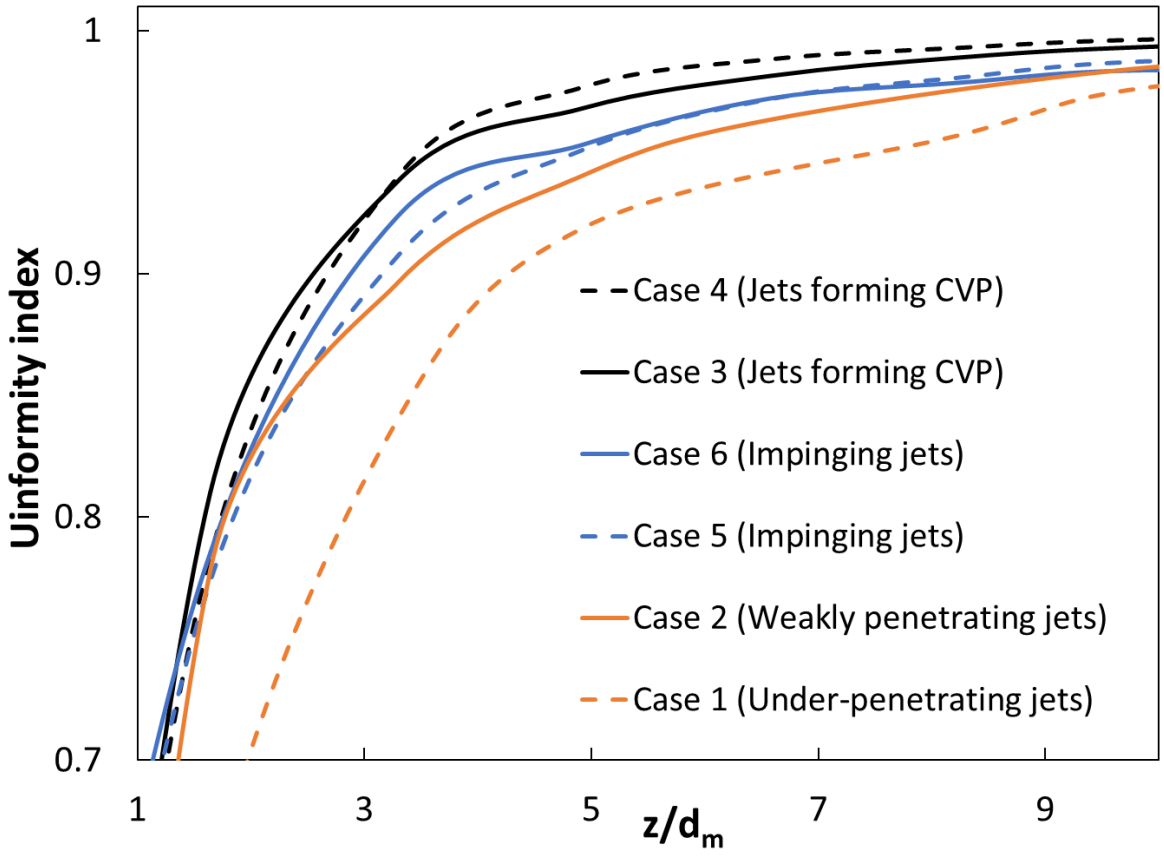

Figure 5. UI along the dimensionless axial distance showing mixing performance for different MJC designs. The jets forming CVP leads to the fastest mixing.

The slow mixing for this case may be attributed to the absence of vortex structures and lower diffusion area available for mixing of the fluids. Since under-penetrating jet "sticks" to the walls of the cylinder (see Figure 3), most of the benzene injected does not instantly meet the crossflow of water. This reduces the area of contact between the two fluids and, thus, the molecular diffusion of benzene into the water as governed by equation 16. Improvement in mixing is observed with the penetration of jets in the cross-flow (greater *r*). The weakly penetrating jets (case 2) perform better than under-penetrating jets due to increase in diffusion area with the increased jet penetration. However, a substantial improvement in mixing is observed for jets forming CVP. The fully developed CVPs and the wake structures observed downstream of these jets improve the entrainment and mixing of the fluids [18, 55]. The mixing rate is nearly the same for the two cases with jets forming CVPs (case 3 and case 4). Surprisingly, even with higher turbulence induced in the flow, impinging jets (case 5 and case 6) provides slower mixing than jets forming CVP (case 3 and case 4). The absence of coherent vortex structure may be a possible reason for this slow mixing. Moreover, the violent impingement of the jets at the center creates a collimated flow of benzene along the axis of the pipe (see Figure 3), instead of four separate benzene streams observed in jets forming CVP. For the same reagent flow rate, four jets streams will have a larger surface area than a single jet stream. This decrease in effective diffusion area between the fluids leads to slower mixing rate. The turbulence in the IJ case increases the mixing rate of impinging jets more than weakly penetrating jets and under-penetrating jets.

Figure 6 shows the instantaneous contours of the mass fraction of benzene at some cross-sections along the length of the tube. As expected, the under-penetrating jet (case 1) sticks close to the walls of the tube as a large concentration of benzene exists near the wall. The mixing of

benzene is mainly governed by molecular diffusion. The increase in the diffusion area with better jet penetration can be clearly seen for the jets forming CVP (case 3 and case 4). The distribution

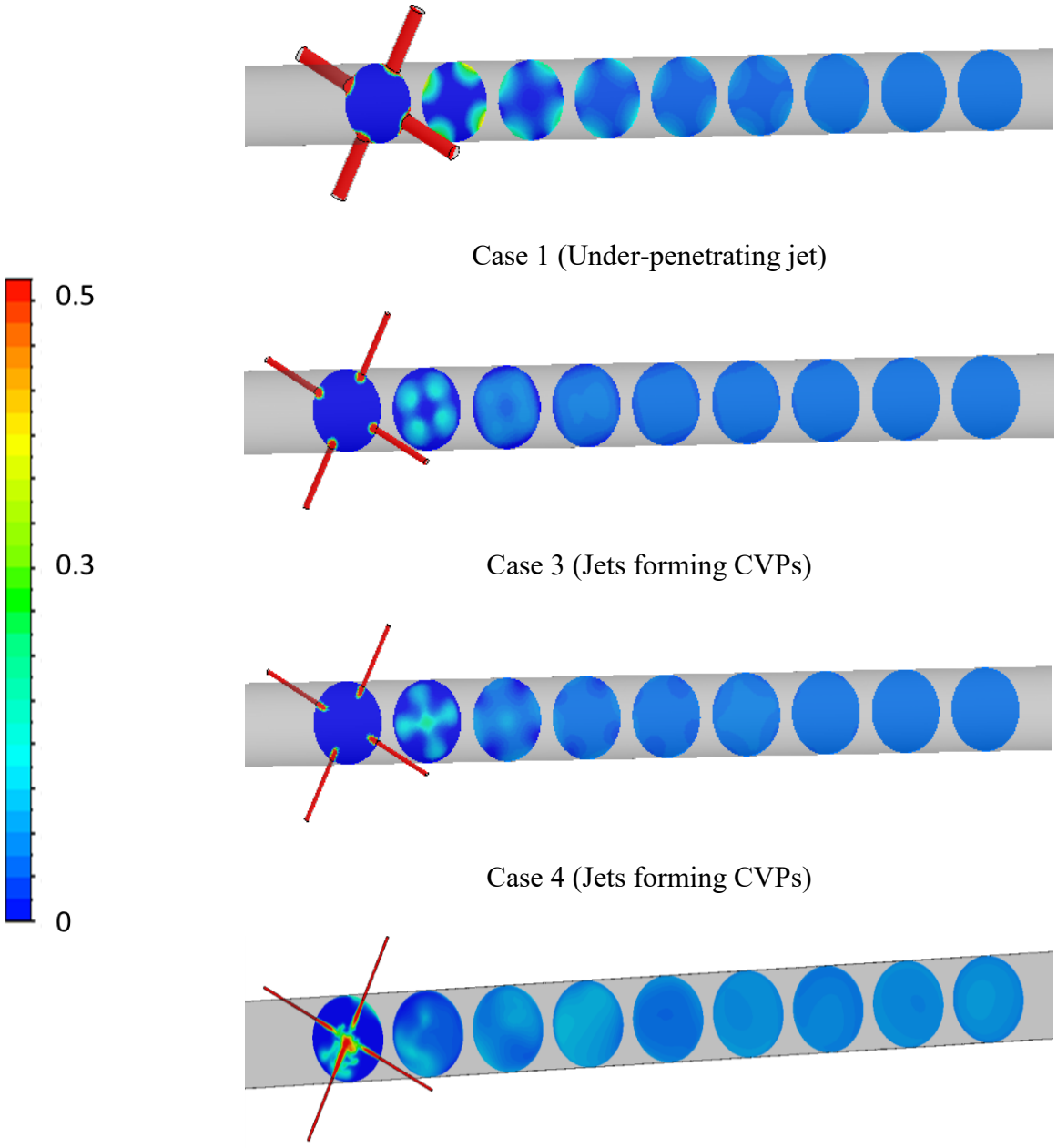

Figure 6. Instantaneous contours of the mass fraction at some cross-section along the main pipe. The figure shows the different mixing mechanism dominant in the four cases.

of benzene is almost uniform by the sixth cross-section shown in Figure 6. However, note the difference in benzene distribution just after the injection plane for case 3 and case 4. Most of the jet mass flow passes in-line with the jet injection nozzle for case 3 as the strength of CVP is weak (see Figure 3). However, for case 4, the strength of CVPs improve due to increasing jet velocity; most of the benzene mass flow is swept with the CVP. This gives a higher mass flux of benzene at almost 45º to the jet axis. Higher concentration of benzene is also seen near the pipe axis. For the impinging jet, the distribution of benzene concentration is random and turbulent diffusion drives the mixing process. A lot of small-scale eddies are continuously generated and dissipated at the vicinity of the impingement point. These small-scale eddies help increase the diffusion area between the fluids and improve the mixing rate. However, the mixing is slower than the jets forming CVPs as the turbulence from the jet is dissipated in the overall laminar pipe flow.

The above results show the optimization of MJC mixer for a single set of fluids at a fixed operating condition. Scaling of such mixer designs can help to generalize the results for wide range of fluids and operating conditions. It can help design and optimize future mixers with minimum simulations and experiments. **Figure 7-a** compares the dimensionless mixing length for three uniformity indices with the velocity ratio of the jets. Mixing length is defined as the distance along the main pipe required to achieve the specified time averaged uniformity index. Even for the same velocity ratio (0.22 and 2.73) the mixing lengths differ by more than 20% for a solution uniformity of 0.95. Also, there is no observable correlation between the mixing length and velocity ratio. Velocity ratio is a very simplistic to define such a complicated flow. It contains information only about the relative inertial force between the two fluids. However, viscous forces and the density of fluids also play a major role in the development of such flows. *Re* number of the flow contains information about the inertial as well as the viscous forces of the fluids. **Figure 7-b** shows the

same dimensionless mixing length for the specified solution uniformity vs the *Re* ratio of crossflow to jet. As the *Re* of the jet increases the mixing length decreases due to better jet penetration. It reaches a local minimum at the location where the jets form counter rotating vortices. Further increase in *Re* leads to a decrease in the mixing length as the jets start to impinge. Therefore, *Re* ratio may be a better non-dimensional parameter to quantify performance of an MJC mixer. However, a more extensive study including more data points with change in fluids properties should be done to test this hypothesis.

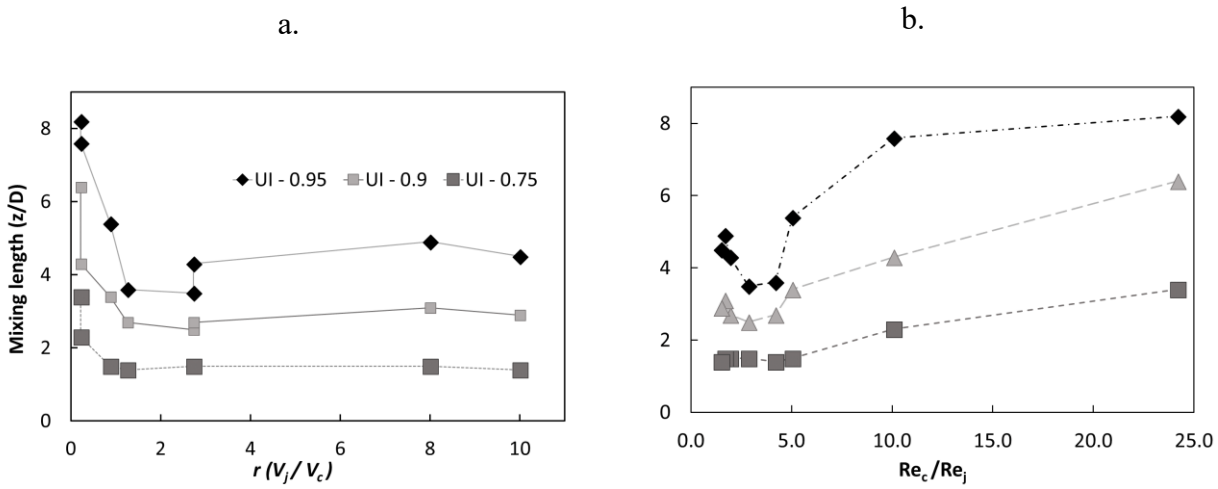

Figure 7. Mixing length for 0.75, 0.90, and 0.95 solution uniformity vs (a) velocity ratio and (b) *Re* ratio. *Re* ratio is better is categorizing the mixing length for the cases simulated. It shows a local minimum for jets forming CVPs.

4.3 Study of Methanol Decomposition in Supercritical Water Reactor

Table 4. The boundary condition for modeling MeOH decomposition

Average Temp in the Reactor (K)	Mass Flow Rate of Water (g/s)	Residence Time (s)	Reynolds Number
653	0.058	100.0	384
683	0.042	94.3	422
719	0.050	21.6	652

First-order chemical kinetics rate parameters based on data of Hack et al. [26], were used in a CFD calculation to study the influence of finite rate mixing on the decomposition methanol. Table 4 shows the conditions used in the CFD simulation. The low *Re* suggests laminar flow conditions for all cases. MeOH is injected in to crossflow via MJC mixer with four radial nozzles ID 0.25 mm. Due to the flow symmetry, the computational domain that consists of a quadrant section of the 3D domain (see Figure 2) was used. Domain length is based on the residence time required for complete decomposition of MeOH at each temperature.

Figure 8 compares the MeOH decomposition rate predicted by CFD with the experimental data of Hack et al. [54]. The normalized concentration of MeOH for the CFD is evaluated at

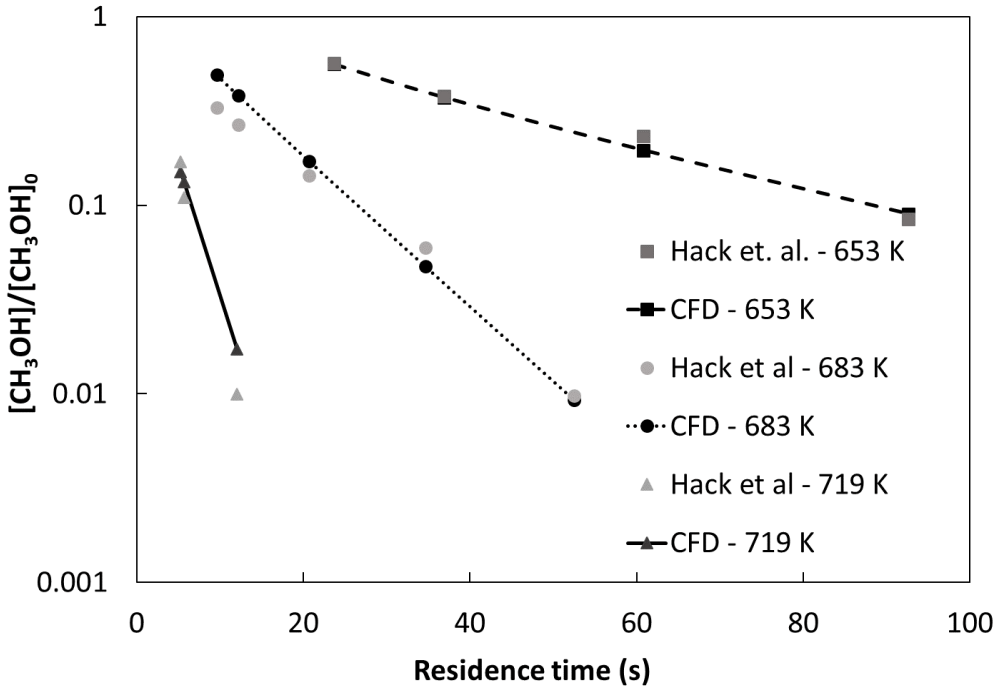

Figure 8. MeOH decomposition at different reactor temperatures from CFD compared with the data [54].

various cross-sections of the domain corresponding to the experimental residence times for each temperature. $[CH_3OH]_0$ is the initial concentration of MeOH based on the mass flow rates of MeOH and water. The predicted MeOH concentration is in close agreement with the experimental data, which indicates that finite-rate mixing does not influence the overall MeOH destruction under these conditions. The main reason for this is the slow chemical rate relative to the mixing rate. The effect of the mixing rate on the overall reaction can, however, be significant for slow mixing and fast chemical rates. The relationship between the mixing and kinetic rates can be described by the global and local Damkohler (Da) and Karlovitz (Ka) numbers, which are often used in combustion

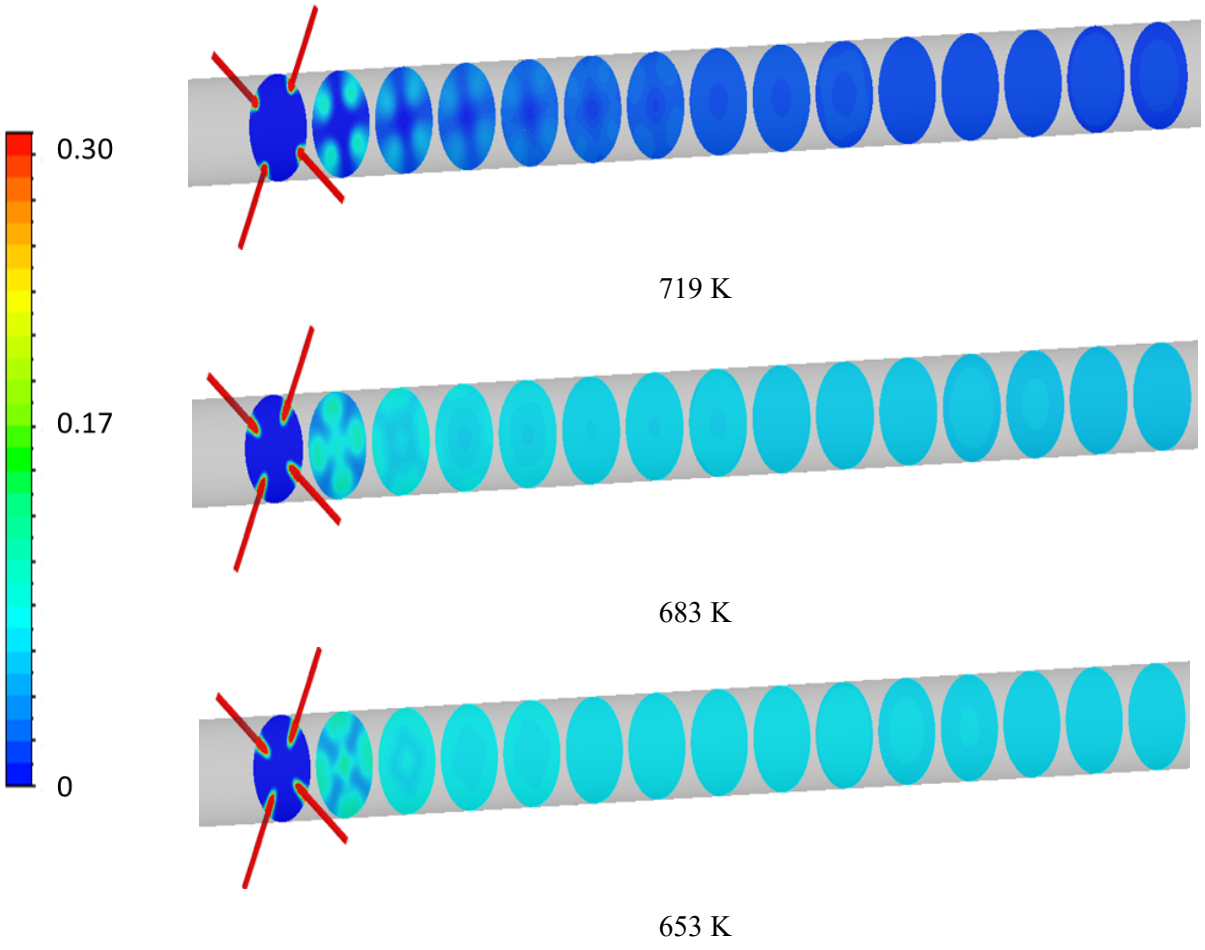

Figure 9. Instantaneous contours of methanol mass fraction for several cross-sections of the reactor. At lower temperatures, uniform mixture composition is obtained before methanol reacts with the crossflow.

modeling, e.g., [56]. In the CFD simulations, the competition between the mixing and chemical kinetic rates in the presence of turbulence can be evaluated using a model describing turbulence-chemistry interaction, e.g., the eddy-break-up model or the eddy dissipation concept as presented in combustion literature [57, 58].

Figure 9 shows the mass fraction contours of MeOH at several cross-sections along the length of the tube. At low temperatures (653 K and 683 K), a uniform mixture composition is achieved within a few diameters of the tube. MeOH mixes uniformly in the reactor section giving plug flow conditions in the reactor; the measured kinetic rates would be independent of the mixing rate for such scenario. However, the kinetic rate of the reaction is considerably higher at 719 K, and large areas of high methanol concentration are located near the injection plane. In this scenario, the mixing rate is of the same order as the chemical reaction rate at 719 K.

Figure 10 shows the contours of the CO_2 mass fraction in the reactor, which is one of the products of the reaction. The concentration of CO_2 shows the regions in the reactor where the chemical reaction is actively proceeding forward. Nearly uniform concentration of CO_2 is observed for all cross-section of the reactor at 653 K. The kinetic reaction rate is substantially lower than the mixing rate; confirming the plug flow condition in the reactor shortly after the injection of MeOH. At 653 K the plug flow assumption is still valid as a uniform CO_2 concentration is observed 3-4 plane away from the injection point. However, moving further away a high concentration of benzene is seen closer to the walls as laminar flow regime develops in the pipe. For fully developed laminar flow, the residence time closer to the walls is higher due to lower flow velocity in the boundary layer. In the kinetic rate studies with *in-situ* measurements, laminar flow conditions in the pipe can introduce significant errors in the measurements, depending on the position of the probe in the cross-section of the pipe. Careful data analysis is required for interpreting such data;

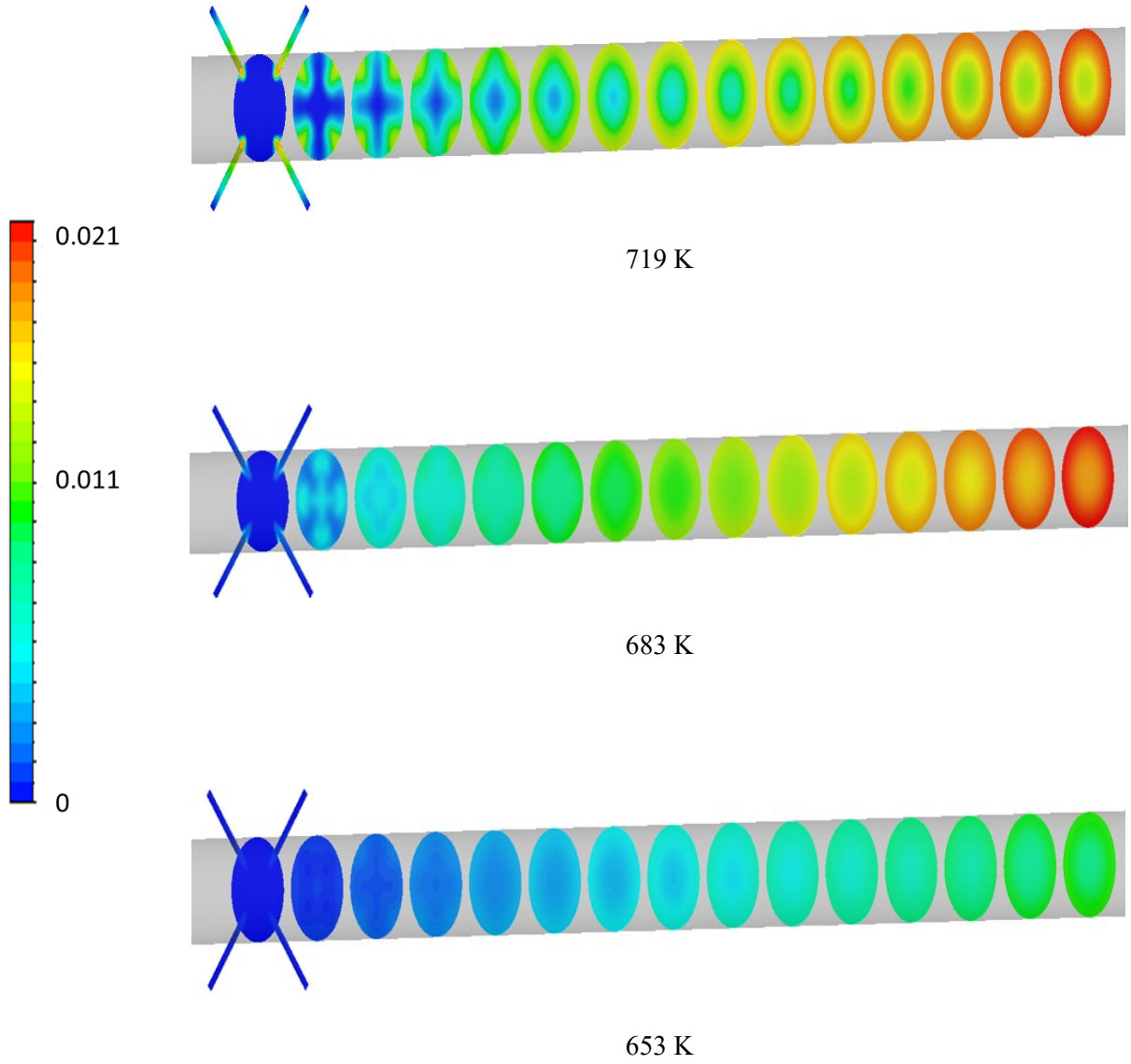

Figure 10. Instantaneous contours of mass fraction of CO_2. CO_2 is concentrated near the walls of the reactor at high temperature (719 K) showing that the mixing rate is slower than the chemical reaction rates.

the residence time at the axis of the tube can be two times lower than that calculated by mean velocity. The residence time should be corrected according to the laminar velocity profile. The plug flow condition deviates substantially at 719 K. Mass fraction contours show the localized high concentration of CO_2 at some regions of all the cross-sections. A low concentration of CO_2 is

observed near the axis of the tube due to slow mixing. MeOH reacts before fully mixing with water. While operating the reactor under such conditions, the mixing rate will significantly influence the measured kinetic rates of decomposition reactions.

Figure 11 shows the normalized concentration and UI as a function of residence time in the reactor. The mixing rate is significantly faster than the decomposition rate of MeOH in sc-H_2O, especially at the lower temperatures. UI reaches 90% in less than 2 sec, while for rates based on Hack et al. data, it takes more than 30 secs for 50% decomposition at 683 K and 10 secs at 653 K. However, at 719 K, the reaction rate of MeOH becomes comparable to the mixing rate. Since 50% of the MeOH has already reacted at UI~0.8, the plug flow assumptions are not valid in this operational condition. An experimentally determined reaction rate at such conditions can be

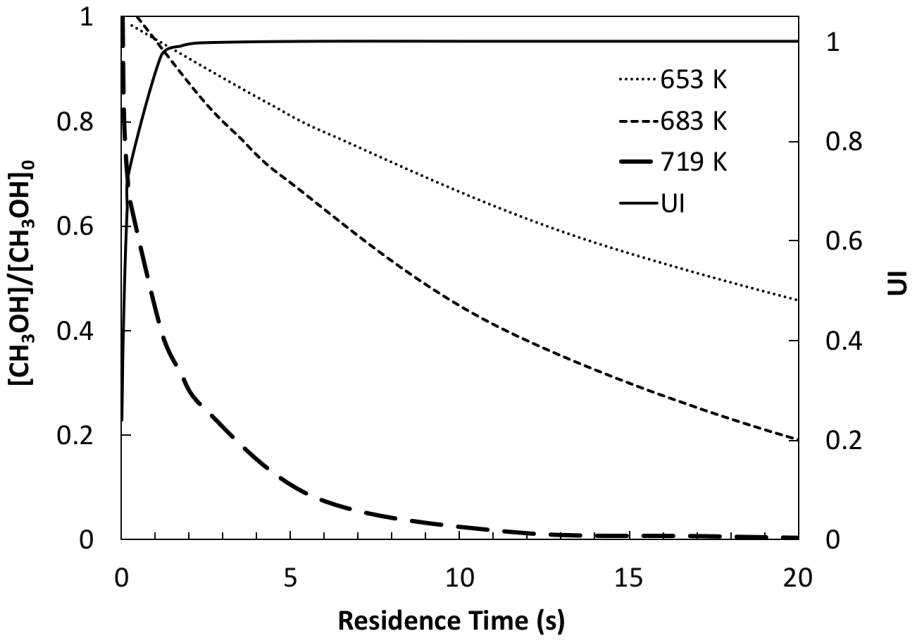

Figure 11. Uniformity Index and the MeOH concentration vs. the residence time in the reactor. The mixing time is approximately 1 s, which is significantly less than the characteristic chemical time for low temperatures.

considerably affected by the mixing rate. The decomposition rate of MeOH in sc-H_2O is moderate compared to other organic molecules. For example, the reaction rate of glucose and glycerol are an order magnitude greater than for MeOH [36]. Therefore, for high temperatures and compounds with rapid decomposition, the mixing section design becomes critical.

Chapter 5. Conclusions

Mixing and decomposition of organic compounds in supercritical water was studied with CFD. Kinetic theory was used to evaluate the diffusion coefficient and viscosity of a benzene and water mixture. The model shows good agreement with published properties at low pressures (25MPa), allowing its use in practical applications. The mixing of supercritical fluids in an MJC mixer was studied using DDES CFD simulations. The velocity ratio of the jets to crossflow was varied by changing the diameter of the jets. The best mixing occurs at an optimum velocity ratio when jets form CVPs downstream of the injection location. Low velocity-ratios give slow mixing as the jets under-penetrate the bulk flow. At higher velocity ratios, the jets impinge, resulting in the formation of a single jet and reducing the available diffusion surface area. Decomposition of MeOH was modeled. With MJC the mixing rate was considerably faster than the decomposition rate of MeOH at lower temperatures. At higher temperatures, the kinetic rate becomes comparable to the mixing rate. Plug flow assumptions may not be valid in situations of slow mixing and fast chemical kinetic rates. For such scenarios, the mixing section should be carefully designed for fast mixing. The computational modeling approach described can be used for the design and optimization of supercritical fluids reactors.

Appendix

A.1 Methods to predict viscosity near supercritical point

Kinetic theory of gases serves as simple and effective tool to predict properties of gases at high temperature and low pressures. Essential when the compressibility factor is close to unity and ideal gas behavior exists. However, kinetic theory cannot model the viscosity of fluids close to the critical point. **Figure 12** compares the viscosity predicted by modified kinetic theory (see equation 4) with NIST database [46]. The viscosity predictions are independent of the gas pressure. The predicted and the published viscosity are in close agreement away from the critical point. However, it shows that kinetic theory cannot predict the sharp change in properties close to the critical point.

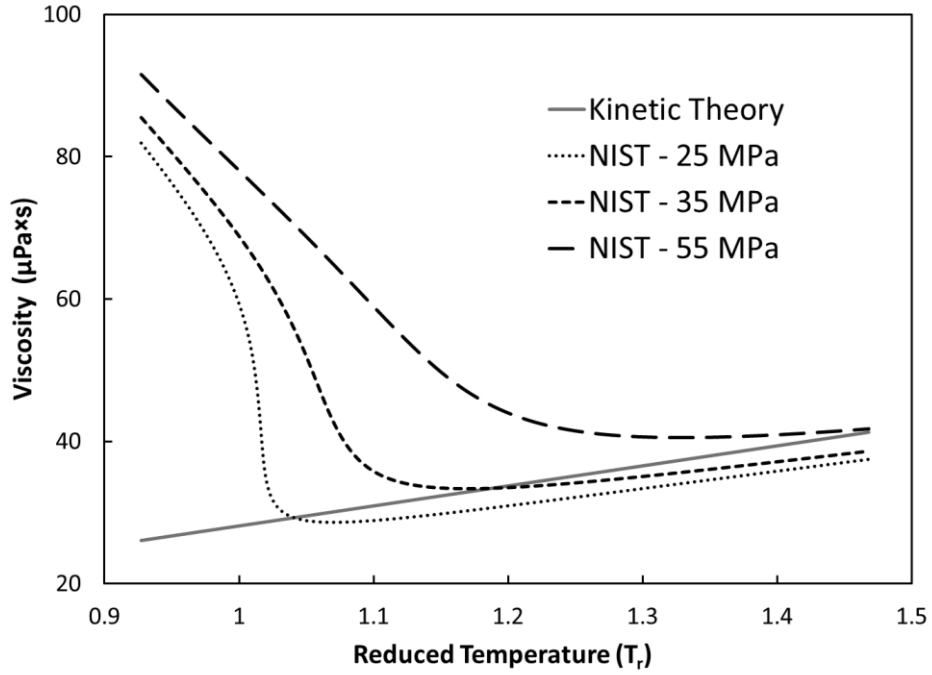

Figure 12. Viscosity of water predicted by kinetic theory compared with the NIST database. The viscosity prediction agrees closely with the data at low pressure and away from the critical point.

The error in viscosity prediction is less than 5% at $1.03 < T_r < 1.07$ and 25 MPa. Away from the critical point the maximum error is less than 10% at 25 MPa and 35 MPa. However, the error increases at 55 MPa as the properties of the fluid become closer to that of liquid [43] and kinetic theory of gases is not applicable at high reduced pressures. The errors in viscosity predictions also increase with the increase in reduced pressure of the fluids.

Many authors have suggested more sophisticated methods to improve the viscosity predictions close to the critical point [43]. These methods are either based on the modified Chapman-Enskog theory or the law of corresponding states [43]. Modified Chapman-Enskog theory is explained in Chapter 2. Kinetic Theory Model It is based on hard sphere theory with corrections for molecular interactions. Most methods correct these methods by introducing additions tuning parameters. The theorem of corresponding states correlates the fluid properties to the reduced pressure and reduced temperature of the gases. It depends on the premise that the at same the reduced temperature and pressure the gases have the same compressibility factor and they deviate equally from the ideal gas behavior.

Chung et al. proposed a method based on the modified Chapman-Enskog theory to predict the viscosity of gases [59]. It contains additional tuning parameters like the acentric factor and dipole moment of the fluid. Though, the method is not applicable for quantum gases. Luckas et al. proposed a more involved method based on the method of corresponding states [60]. The correction factors depend on the dipole moment of the gases. However, the method gives considerable deviation for highly associated molecules [43]. **Figure 13** compares the viscosity of water available in the NIST database with the viscosity predicted by kinetic theory method, method of Lucas et al., and the method of Chung et al. As discussed before, the kinetic theory predictions deviate significantly near the critical point. The other two methods do a much better job in

predicting viscosity close to the critical point. Method of Lucas et al. gives closest agreement with the NIST database at low pressure. At high temperatures ($T_r > 1.2$), the error is less than 3% at 250 bars and 350 bars. However, a considerable deviation is observed at high reduced pressures ($P_r > 2$) for method of Lucas and method of Chung, especially close to the critical point. The predictions by method of Chung compare better at high reduced pressures than the method of Lucas. At high reduced pressure, properties of supercritical fluid become closer to that of liquid and these methods are not longer application. At such high reduced pressure, other methods more suitable for estimating liquid viscosities should be used [43].

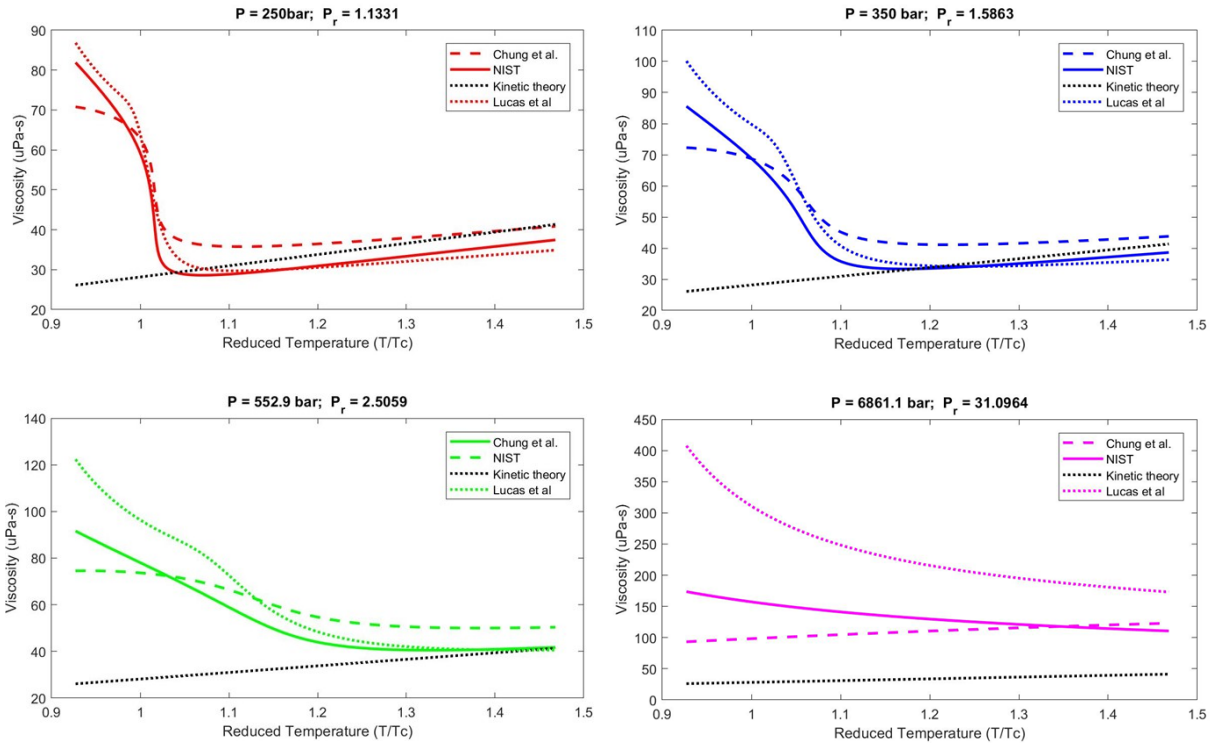

Figure 13. Comparison of viscosity predictions by method of Lucas et al., method of Chung et al., and the kinetic theory method with the NIST database [46]. Predictions by method of Lucas compare best with the NIST database at low pressures.

A.2 Effect of number of jets on mixing

It has been found that the mixing efficiency of an MJC mixer improves with increase in number of jets until it reaches a threshold. Further increase in number of jets leads to a decrease in mixing due to impingement of jets [13-15, 26]. Aklilu et al. found that four jet MJC gives a considerably superior performance than MJC with lesser number of jets [61].

To understand the influence of number of jets on the mixing rate of MJC mixer, CFD simulations were performed with two and four jets. Each configuration was simulated with 0.25 mm and 0.5 mm jet diameters. The domain and boundary conditions were same as explained in Chapter 3. Computational Model However, an unsteady RANS scheme models the flow instabilities and possible transition to turbulence.

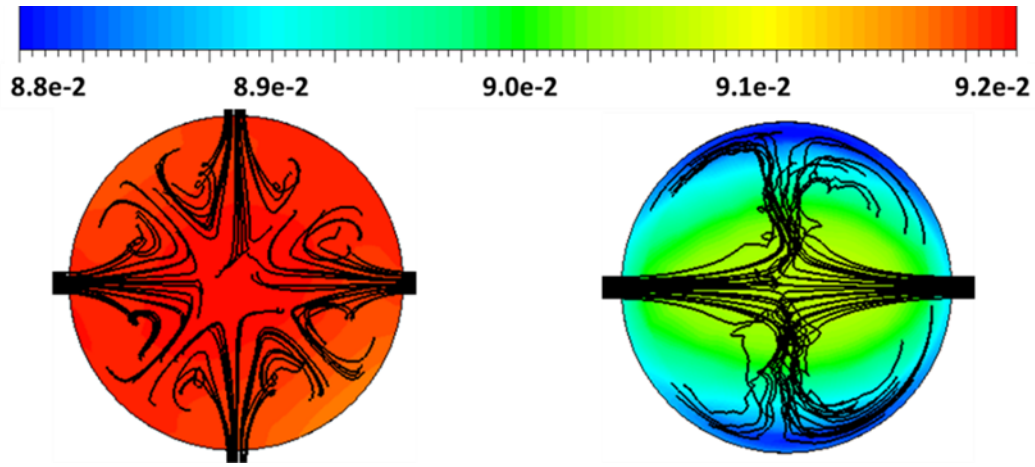

Figure 14. Flow pathlines originating from the jet inlets along with mass fraction contours of benzene at 50 mm from the injection plane. The diameter of the jets is 0.25 mm. The benzene jets impinge with the two jet configuration and forms a high benzene concetration region at the center.

Figure 14 shows the flow path-lines originating from the jet inlets along with mass fraction contours of benzene at 50 mm from the injection plane. The diameter of the jets is 0.25 mm. Four pairs of counter-rotating vortices are formed with the four-jet MJC. The four-jet MJC also gives a better initial distribution of benzene at the injection plane. For the same mass flow rate, the jet velocity is higher for two-jet MJC due to a lower cross section area. Therefore, the benzene jets impinge at the center for two-jet MJC. The mass fraction contours show a higher concentration of benzene around the impingement point for the two-jet MJC. The four-jet MJC gives a substantially better mixing as shown by the uniform mass fraction contour.

$$Convective\ time\ (t) = \frac{Axial\ distance}{|\overrightarrow{v_z}|} \tag{18}$$

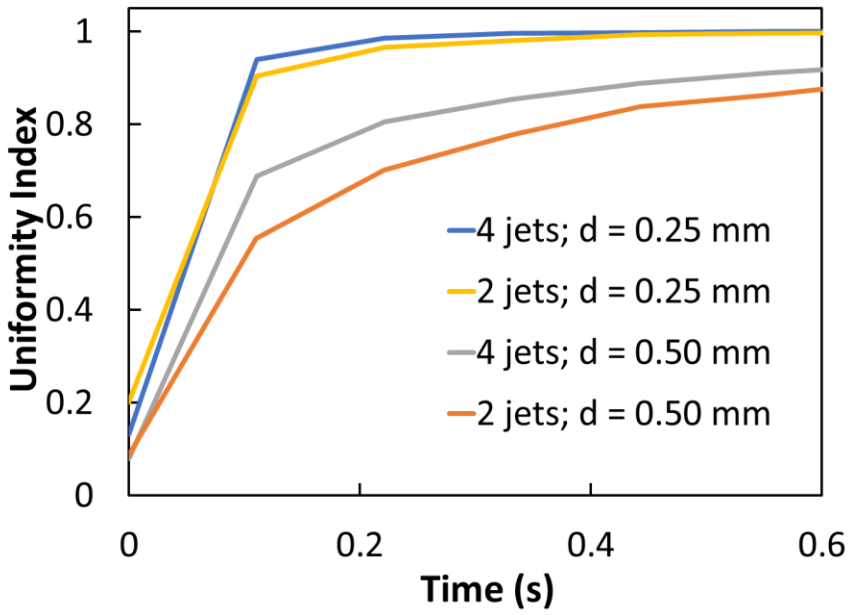

Figure 15. UI of benzene vs. the residence time in the reactor from the injection point. The mixing rate is faster with four jets than two jets for both the jet diameters.

Equation 18 gives the convective time along the crossflow. It corresponds to the residence time of the flow from the jet injection plane. It can help to quantify the mixing time of the fluid in the reactor. **Figure 15** shows the uniformity index of benzene along the convective time for the two-jet and four-jet MJC with specified jet diameter. For both the jet diameters, four jets give faster mixing than two jets. The four-jet MJC divides the same mass flow of benzene into four streams. Therefore, the diffusion area between Sc-H_2O and benzene is larger in four-jet MJC than two-jet MJC. The mixing time for both the configuration reduces with the decrease in jet diameter due to improved jet penetration.

References

[1] P. E. Savage, "Organic chemical reactions in supercritical water," *Chemical Reviews,* vol. 99, no. 2, pp. 603-621, 1999.

[2] H. Weingärtner and E. U. Franck, "Supercritical Water as a Solvent," (in en), *Angewandte Chemie International Edition,* vol. 44, no. 18, pp. 2672-2692, 2005/04/29/ 2005.

[3] M. J. Antal Jr, S. G. Allen, D. Schulman, X. Xu, and R. J. Divilio, "Biomass gasification in supercritical water," *Industrial and Engineering Chemistry Research,* vol. 39, no. 11, pp. 4040-4053, 2000.

[4] P. Savage, Q. Guan, and C. Huelsman, "Biomass gasification in supercritical water," *Abstr. Pap. Am. Chem. Soc.,* vol. 244, 2012.

[5] F. Ondze, O. Boutin, J.-C. Ruiz, J.-H. Ferrasse, and F. Charton, "Supercritical water gasification of beet residues: From batch to continuous reactor," *Chemical Engineering Science,* vol. 123, pp. 350-358, 2/17/ 2015.

[6] N. Aoki, D. Hojo, S. Takami, and T. Adschiri, "Chapter 5 - Environmentally Benign Route for Nanomaterial Synthesis by Using SCW," in *Supercritical Fluid Technology for Energy and Environmental Applications*, V. Anikeev and M. Fan, Eds. Boston: Elsevier, 2014, pp. 99-110.

[7] L. Wang *et al.*, "Oxidation of chemical warfare agents in supercritical water," vol. 356-360, ed, 2012, pp. 2610-2615.

[8] B. Pinkard *et al.*, "In-Situ Raman Spectroscopy to Study Supercritical Water Gasification of Formic Acid," presented at the 12th International Symposium on Supercritical Fluids Antebes, France, 2018.

[9] P. A. Marrone and G. T. Hong, "Corrosion control methods in supercritical water oxidation and gasification processes," *The Journal of Supercritical Fluids,* vol. 51, no. 2, pp. 83-103, 12// 2009.

[10] R. K. Helling, "Oxidation Kinetics of Simple Compounds in Supercritical Water: Carbon Monoxide, Ammonia and Ethanol," MIT, 1986.

[11] G. James, H. Arne, and K. Aman, "A review of passive and active mixing systems in microfluidic devices," *International Journal of Multiphysics,* vol. 1, no. 1, 2007.

[12] K. Mahesh, "The Interaction of Jets with Crossflow," *Annu. Rev. Fluid Mech.,* vol. 45, pp. 379-407, 2013.

[13] P. Luo, H. Jia, C. Xin, G. Xiang, Z. Jiao, and H. Wu, "An experimental study of liquid mixing in a multi-orifice-impinging transverse jet mixer using PLIF," *Chemical Engineering Journal,* vol. 228, pp. 554-564, 2013/07/15/ 2013.

[14] P. C. Luo, Y. Fang, B. Wu, and H. Wu, "Turbulent Characteristics and Design of Transverse Jet Mixers with Multiple Orifices," *Ind. Eng. Chem. Res.,* vol. 55, no. 32, pp. 8858-8868, 2016.

[15] J. D. Holdeman, D. Liscinsky, V. Oechsle, G. Samuelsen, and C. E. Smith, "Mixing of multiple jets with a confined subsonic crossflow .1. Cylindrical duct," *J. Eng. Gas. Turbines Power-Trans. ASME,* vol. 119, no. 4, pp. 852-862, 1997.

[16] L. L. Yuan, R. L. Street, and J. H. Ferziger, "Large-eddy simulations of a round jet in crossflow," *Journal of Fluid Mechanics,* vol. 379, pp. 71-104, 1999.

[17] L. K. Su and M. G. Mungal, "Simultaneous measurements of scalar and velocity field evolution in turbulent crossflowing jets," *J. Fluid Mech.,* vol. 513, pp. 1-45, 2004.

[18] A. R. Karagozian, "The jet in crossflow," *Physics of Fluids,* vol. 26, no. 10, p. 101303, 2014.

[19] R. Sau and K. Mahesh, "Passive scalar mixing in vortex rings," *J. Fluid Mech.,* vol. 582, pp. 449-461, 2007.

[20] R. M. Kelso, T. Lim, and A. E. Perry, "An experimental study of round jets in cross-flow," *J. Fluid Mech.,* vol. 306, pp. 111-144, 1996.

[21] R. Sau and K. Mahesh, "Dynamics and mixing of vortex rings in crossflow," (in en), *Journal of Fluid Mechanics,* vol. 604, 2008/06// 2008.

[22] M. S. Acarlar and C. R. Smith, "A study of hairpin vortices in a laminar boundary layer. Part 2. Hairpin vortices generated by fluid injection," *J. Fluid. Mech.,* vol. 175, no. -1, pp. 43-83, 1987.

[23] S. Muppidi and K. Mahesh, "Direct numerical simulation of passive scalar transport in transverse jets," *J. Fluid Mech.,* vol. 598, pp. 335-360, 2008.

[24] T. Fric and A. Roshko, "Vortical structure in the wake of a transverse jet," *J. Fluid Mech.,* vol. 279, pp. 1-47, 1994.

[25] M. F. Urson, M. J. Lightstone, and H. Thomson, "A Numerical Study of Jets in a Reacting Crossflow," *Numerical Heat Transfer, Part A: Applications,* vol. 40, no. 7, pp. 689-714, 2001.

[26] J. T. Kroll, W. A. Sowa, G. S. Samuelsen, and J. D. Holdeman, "Optimization of Orifice Geometry for Crossflow Mixing in a Cylindrical Duct," *Journal of Propulsion and Power,* vol. 16, no. 6, pp. 929-938, 2000/11/01 2000.

[27] E. Kartaev, V. P. Lukashov, S. Vashenko, S. M. Aulchenko, O. Kovalev, and D. V. Sergachev, "An Experimental Study of the Synthesis of Ultrafine Titania Powder in Plasmachemical Flow-Type Reactor," *Int. J. Chem. React. Eng.,* vol. 12, no. 1, 2014.

[28] E. V. Kartaev, V. A. Emelkin, M. G. Ktalkherman, S. M. Aulchenko, S. P. Vashenko, and V. I. Kuzmin, "Formation of counter flow jet resulting from impingement of multiple jets radially injected in a crossflow," *Experimental Thermal and Fluid Science,* vol. 68, pp. 310-321, 2015/11/01/ 2015.

[29] P.-c. Luo, Y. Cheng, Y. Jin, W.-h. Yang, and J.-s. Ding, "Fast liquid mixing by cross-flow impingement in millimeter channels," *Chemical Engineering Science,* vol. 62, no. 22, pp. 6178-6190, 2007/11/01/ 2007.

[30] S. J. Wang and A. S. Mujumdar, "Flow and mixing characteristics of multiple and multi-set opposing jets," *Chemical Engineering and Processing: Process Intensification,* vol. 46, no. 8, pp. 703-712, 2007/08/01/ 2007.

[31] S. Acharya, M. Tyagi, and A. Hoda, "Flow and heat transfer predictions for film cooling," (in eng), *Ann N Y Acad Sci,* vol. 934, pp. 110-25, May 2001.

[32] P. R. Spalart, S. Deck, M. L. Shur, K. D. Squires, M. K. Strelets, and A. Travin, "A New Version of Detached-eddy Simulation, Resistant to Ambiguous Grid Densities," *Theoretical and Computational Fluid Dynamics,* journal article vol. 20, no. 3, p. 181, May 30 2006.

[33] S. Schmidt and F. Thiele, "Detached Eddy Simulation of Flow around A-Airfoil," *Flow, Turbulence and Combustion,* vol. 71, no. 1, pp. 261-278, 2003.

[34] P. R. Spalart, "Detached-eddy simulation," *Annual review of fluid mechanics,* vol. 41, pp. 181-202, 2009.

[35] Z. Yin and P. Durbin, "Adaptive Detached Eddy Simulation of Jet in Cross Flow," in *55th AIAA Aerospace Sciences Meeting*(AIAA SciTech Forum: American Institute of Aeronautics and Astronautics, 2017.

[36] B. R. Pinkard, D. J. Gorman, K. Tiwari, J. C. Kramlich, P. G. Reinhall, and I. V. Novosselov, "Review of Gasification of Organic Compounds in Continuous-Flow, Supercritical Water Reactors," *Industrial & Engineering Chemistry Research,* vol. 57, no. 10, pp. 3471-3481, 2018/03/14 2018.

[37] K. Tiwari, B. Pinkard, D. Gorman, J. Davis, J. Kramlich, and I. Novosselov, "Computational Modeling of Mixing and Gasification in Continuous-Flow Supercritical Water Reactor," presented at the 12t^{h} International Symposium on Supercritical Fluids, Antibes, France, 2018.

[38] C. Nieto-Draghi, J. Bonet Avalos, O. Contreras, P. Ungerer, and J. Ridard, "Dynamical and structural properties of benzene in supercritical water," (in eng), *The Journal of Chemical Physics,* vol. 121, no. 21, pp. 10566-10576, 2004/12/01/ 2004.

[39] A. Plugatyr and I. M. Svishchev, "Molecular Diffusivity of Phenol in Sub- and Supercritical Water: Application of the Split-Flow Taylor Dispersion Technique," (in en), *The Journal of Physical Chemistry B,* vol. 115, no. 11, pp. 2555-2562, 2011/03/24/ 2011.

[40] F. M. Mourits and F. H. A. Rummens, "A critical evaluation of Lennard–Jones and Stockmayer potential parameters and of some correlation methods," (in en), *http://dx.doi.org/10.1139/v77-418*, 04 February 2011 2011.

[41] C. F. Curtiss, R. B. Bird, L. University of Wisconsin. Naval Research, and J. O. Hirschfelder, *Molecular theory of gases and liquids*. New York: New York : Wiley, 1954.

[42] S. Chapman, *The mathematical theory of non-uniform gases; an account of the kinetic theory of viscosity, thermal conduction, and diffusion in gases*. Cambridge [England: Cambridge England University Press, 1939.

[43] B. E. Poling, *The properties of gases and liquids*, 5th ed. ed. New York: New York : McGraw-Hill, 2001.

[44] I. Medina, "Determination of diffusion coefficients for supercritical fluids," *Journal of Chromatography A,* vol. 1250, pp. 124-140, 2012.

[45] C.-H. He and Y.-S. Yu, "New equation for infinite-dilution diffusion coefficients in supercritical and high-temperature liquid solvents," *Industrial and Engineering Chemistry Research,* vol. 37, no. 9, pp. 3793-3798, 1998.

[46] E. W. Lemmon, M. O. McLinden, and D. G. Friend, "NIST Chemistry WebBook, NIST Standard Reference Database Number 69," E. P. J. Linstrom and W. G. Mallard, Eds. Gaithersburg MD.

[47] "*ANSYS® Academic Research Fluent, Release 18.2*," ed.

[48] P. R. Spalart *et al.*, "Comments on the Feasibility of LES for Wings, and on a Hybrid RANS/LES Approach," ed: Greyden Press, 1997, pp. 137-148.

[49] C. Mockett, M. Fuchs, and F. Thiele, "Progress in DES for wall-modelled LES of complex internal flows," *Computers & Fluids,* vol. 65, pp. 44-55, 2012/07/30/ 2012.

[50] K. Hanjalić, D. Borello, G. Delibra, and F. Rispoli, "Hybrid LES/RANS of internal flows: A case for more advanced RANS," *Notes on Numerical Fluid Mechanics and Multidisciplinary Design,* vol. 130, pp. 19-35, 2015.

[51] S. B. Pope, *Turbulent flows*, Repr. with corrections. ed. Cambridge ; New York: Cambridge ; New York : Cambridge University Press, 2003.

[52] D. C. Wilcox, *Turbulence Modelig for CFD*. DCW Industries, Inc., 2006.

[53] X. Xiao, J. R. Edwards, and H. A. Hassan, "Blending Functions in Hybrid Large-Eddy/Reynolds-Averaged Navier-Stokes Simulations," (in en), *http://dx.doi.org/10.2514/1.2094,* research-article 2012-05-02 2012.

[54] W. Hack, D. Masten, and S. J. Buelow, "Methanol and ethanol decomposition in supercritical water," *Z. Phys. Chemie-Int. J. Res. Phys. Chem. Chem. Phys.,* vol. 219, no. 3, pp. 367-378, 2005.

[55] S. Smith and M. G. Mungal, "Mixing, structure and scaling of the jet in crossflow," *J. Fluid Mech.,* vol. 357, pp. 83-122, 1998.

[56] Y. Guan and I. Novosselov, "Damkohler Number Analysis in Lean Blow-Out of Toroidal Jet Stirred Reactor," *Journal of Engineering for Gas Turbines and Power,* vol. Accepted no. GTP-17-1495, March 2018.

[57] M. F. Karalus, K. B. Fackler, I. V. Novosselov, J. C. Kramlich, and P. C. Malte, "Characterizing the mechanism of lean blowout for a recirculation-stabilized premixed hydrogen flame," in *ASME*

Turbo Expo 2012: Turbine Technical Conference and Exposition, 2012, pp. 21-30: American Society of Mechanical Engineers.

[58] I. V. Novosselov and P. C. Malte, "Development and application of an eight-step global mechanism for CFD and CRN simulations of lean-premixed combustors," *Journal of Engineering for Gas Turbines and Power,* vol. 130, no. 2, p. 021502, 2008.

[59] T. H. Chung, L. L. Lee, and K. E. Starling, "Applications of kinetic gas theories and multiparameter correlation for prediction of dilute gas viscosity and thermal conductivity," *Ind. Eng. Chem. Fundam.,* vol. 23, no. 1, 1984.

[60] M. Luckas and K. Lucas, "Transport properties in the zero order gaussian memory function approximation with phase integrals evaluated from Monte Carlo calculations," *Molecular Physics,* vol. 48, no. 5, pp. 989-1002, 1983.

[61] A. T. G. Giorges, L. J. Forney, and X. Wang, "Numerical Study of Multi-Jet Mixing," *Chemical Engineering Research and Design,* vol. 79, no. 5, pp. 515-522, 2001.